

Waveforms and fluxes: Towards a self-consistent effective one body waveform model for nonprecessing, coalescing black-hole binaries for third generation detectors

Angelica Albertini^{1,2}, Alessandro Nagar^{3,4}, Piero Rettegno^{3,5}, Simone Albanesi^{3,5}, and Rossella Gamba⁶

¹*Astronomical Institute of the Czech Academy of Sciences,
Boční II 1401/1a, CZ-141 00 Prague, Czech Republic*

²*Faculty of Mathematics and Physics, Charles University in Prague, 18000 Prague, Czech Republic*

³*INFN Sezione di Torino, Via P. Giuria 1, 10125 Torino, Italy*

⁴*Institut des Hautes Etudes Scientifiques, 91440 Bures-sur-Yvette, France*

⁵*Dipartimento di Fisica, Università di Torino, via P. Giuria 1, 10125 Torino, Italy and*

⁶*Theoretisch-Physikalisches Institut, Friedrich-Schiller-Universität Jena, 07743, Jena, Germany*

We present a comprehensive comparison between numerical relativity (NR) angular momentum fluxes at infinity and the corresponding quantity entering the radiation reaction in **TEOBResumS**, an Effective-One-Body (EOB) waveform model for nonprecessing coalescing black hole binaries on quasi-circular orbits. This comparison prompted us to implement two changes in the model: (i) including Next-to-Quasi-Circular corrections in the $\ell = m$, $\ell \leq 5$ multipoles entering the radiation reaction and (ii) consequently updating the NR-informed spin-orbital sector of the model. This yields a new waveform model that presents a higher self-consistency between waveform and dynamics and an improved agreement with NR simulations. We test the model computing the EOB/NR unfaithfulness $\bar{F}_{\text{EOB/NR}}$ over all 534 spin-aligned configurations available through the Simulating eXtreme Spacetime catalog, notably using the noise spectral density of Advanced LIGO, Einstein Telescope and Cosmic Explorer, for total mass up to $500M_{\odot}$. We find that the maximum unfaithfulness $\bar{F}_{\text{EOB/NR}}^{\text{max}}$ is mostly between 10^{-4} and 10^{-3} , and the performance progressively worsens up to $\sim 5 \times 10^{-3}$ as the effective spin of the system is increased. We perform similar analyses on the **SEOBNRv4HM** model, that delivers $\bar{F}_{\text{EOB/NR}}^{\text{max}}$ values uniformly distributed versus effective spin and mostly between 10^{-3} and 10^{-2} . We conclude that the improved **TEOBResumS** model already represents a reliable and robust first step towards the development of highly accurate waveform templates for third generation detectors.

I. INTRODUCTION

The increasing sensitivity of gravitational-wave (GW) detectors [1, 2] and the associated compact binaries detections [3] motivate work towards physically complete, precise and efficient gravitational-wave models. The effective-one-body (EOB) approach [4–8] is a way to deal with the general-relativistic two-body problem that, by construction, allows the inclusion of perturbative (post-Newtonian, black hole perturbations) and full numerical relativity (NR) results within a single theoretical framework. It currently represents a state-of-art approach for modeling waveforms from binary black holes, conceptually designed to describe the entire inspiral-merger-ringdown phenomenology of quasicircular binaries [9–15] or even eccentric inspirals [16–18] and dynamical captures along hyperbolic orbits [17, 19–21]. An alternative, though less flexible, approach to generate waveforms for detection and parameter estimation relies on phenomenological models, whose latest avatar is **IMRPhenomX** [22–24]. Note however that this kind of waveform models *does rely* on the EOB approach to accurately describe the waveform during the long inspiral, until it is matched to (short) NR simulations.

Currently, there are two families of NR-informed EOB waveform models: the **SEOBNR** family [11, 14] and the **TEOBResumS** [25, 26] family. Both models incorporate precession and tidal effects in some form, but **TEOBResumS** also has spin-aligned versions that can deal with eccentric

inspirals and hyperbolic encounters [17, 20]. Although they are both EOB models, their building blocks are very different, starting from the choice of the underlying Hamiltonians and resummation strategies (see e.g. [27]). The quality of *any* waveform model (specifically, an EOB or a phenomenological one in the current context), is assessed by computing the unfaithfulness (or mismatch) between the waveforms generated by the model and the corresponding NR waveforms over the NR-covered portion of the binary parameter space. This is an obvious procedure since the waveform is the crucial observable that is needed for data analysis. If this is the *only* viable procedure for phenomenological models, for EOB models there are other quantities that might be worth considering. In particular, one has to remember that within the EOB one has access to the *full relative dynamics* of the binary and thus one can complement the waveform comparison with other, gauge-invariant, dynamical quantities. For example, one has access to the gauge-invariant relation between energy and angular momentum [28–30], to the periastron advance [31–33] or, for hyperbolic encounters, to the scattering angle [19].

Together with the Hamiltonian and the waveform, the third building block of any EOB model is the radiation reaction, i.e. the flux of angular momentum and energy radiated via gravitational waves. Surprisingly, the only direct comparison between EOB and NR fluxes, namely Ref. [34], dates back to more than a decade ago. The purpose of this paper is to update Ref. [34] focus-

ing on spin-aligned BBHs. More specifically, it aims at presenting: (i) new calculations of the fluxes from (some of) the spin-aligned NR datasets of the Simulating eXtreme Spacetimes (SXS) catalog [35] and (ii) new EOB/NR comparisons between the fluxes that involve both the most recent version of **TEOBResumS** [12, 13] and **SEOBNRv4HM** [11, 14]. From the EOB/NR flux comparisons with **TEOBResumS**, we learn the importance of including next-to-quasi-circular (NQC) corrections also in the flux modes beyond the $\ell = m = 2$ dominant one in order to achieve a rather high level of consistency ($\lesssim 1\%$) between the EOB and NR fluxes up to merger. By contrast, the EOB/NR flux comparisons with **SEOBNRv4HM** show deficits of this model over the NR-covered portion of the parameter space.

While including NQC factors in the radiation reaction in **TEOBResumS**, we eventually build an improved model, called **TEOBResumS_NQC_1m**, that aims at being more self-consistent and that differs from the standard **TEOBResumS** also for a more precise determination of the NR-informed spin-orbit dynamical parameter. By computing the unfaithfulness for the $\ell = m = 2$ mode over the sample of 534 nonprecessing, quasicircular simulations of the SXS catalog already considered in Ref. [57], we find that both the standard model and the updated one are promising foundations in view of the requirements for third generation detectors [36–41].

The paper is organized as follows. In Sec. II we remind the structure of the radiation reaction within the **TEOBResumS** model, provide a novel computation of the angular momentum flux from (a sample of) NR simulations and compare it with the **TEOBResumS** one. The outcome of this comparisons points to the fact that an improved EOB model would benefit of the inclusion in the flux of NQC corrections beyond the $\ell = m = 2$ ones. This improved model is constructed in Sec. III, notably by providing a new NR-informed fit of the next-to-next-to-next-to-leading-order (NNNLO) effective spin-orbit parameter c_3 previously introduced in [29, 42]. In Sec. IV we assess the accuracy of this NQC-improved model by computing the EOB/NR unfaithfulness using the PSD of advanced LIGO [43], of Einstein Telescope [44, 45] and of Cosmic Explorer [46]. Finally, Sec. V provides a comprehensive comparison between NR, **SEOBNRv4HM** [14, 47, 48] and **TEOBResumS** in its native (i.e. non-NQC-improved) form. We gather our concluding remarks in Sec. VI.

Unless otherwise specified, we use natural units with $c = G = 1$. Our notations are as follows: we denote with (m_1, m_2) the individual masses, while the mass ratio is $q \equiv m_1/m_2 \geq 1$. The total mass and symmetric mass ratio are then $M \equiv m_1 + m_2$ and $\nu = m_1 m_2 / M^2$. We also use the mass fractions $X_{1,2} \equiv m_{1,2}/M$ and $X_{12} \equiv X_1 - X_2 = \sqrt{1 - 4\nu}$. We address with (S_1, S_2) the individual, dimensionful, spin components along the direction of the orbital angular momentum. The dimensionless spin variables are denoted as $\chi_{1,2} \equiv S_{1,2}/(m_{1,2})^2$. We also use $\tilde{a}_{1,2} \equiv X_{1,2}\chi_{1,2}$, the effective spin $\tilde{a}_0 = \tilde{a}_1 + \tilde{a}_2$ and $\tilde{a}_{12} \equiv \tilde{a}_1 - \tilde{a}_2$.

II. GRAVITATIONAL WAVE FLUXES

A. Angular momentum fluxes from Numerical Relativity simulations

In the systematic analysis of fluxes of Ref. [34], performed using NR data from the SXS collaboration, a lot of effort was devoted at the time to remove the spurious oscillations that are present when the flux is expressed in terms of some, gauge-invariant, frequency parameter. The quality of SXS simulations has hugely improved from Ref. [34]. Although SXS data has been used recently in the computation of the fluxes to obtain energy versus angular momentum curves (see e.g. Refs. [28, 29]), an explicit calculation of the flux analogous to the one presented in Ref. [34] has not been attempted again. This is the purpose of this section. Let us start by fixing our notations and conventions. The strain waveform is decomposed in spin-weighted spherical harmonics as

$$h_+ - ih_\times = \frac{1}{D_L} \sum_{\ell} \sum_{m=-\ell}^{\ell} h_{\ell m - 2} Y_{\ell m}(\iota, \phi) \quad (1)$$

where D_L indicates the luminosity distance. The angular momentum flux radiated at infinity reads¹

$$\dot{J}_{\infty} = -\frac{1}{8\pi} \sum_{\ell=2}^{\ell_{\max}} \sum_{m=-\ell}^{\ell} m \Im(\dot{h}_{\ell m} \dot{h}_{\ell m}^*). \quad (2)$$

Here we will consider $\ell_{\max} = 8$. For clarity, we work with the Newton-normalized angular momentum flux

$$\frac{\dot{J}_{\infty}}{\dot{J}_{\text{Newt}}^{\text{circ}}}, \quad (3)$$

where the circularized Newtonian flux formally reads

$$\dot{J}_{\text{Newt}}^{\text{circ}} = \frac{32}{5} \nu^2 (\Omega_{\text{NR}})^{7/3}. \quad (4)$$

Here we define the NR orbital frequency Ω_{NR} simply as

$$\Omega_{\text{NR}} \equiv \frac{\omega_{22}^{\text{NR}}}{2}, \quad (5)$$

where $\omega_{22}^{\text{NR}} \equiv \dot{\phi}_{22}^{\text{NR}}$ is the NR quadrupolar GW frequency and ϕ_{22}^{NR} the phase defined from $h_{22} = A_{22}^{\text{NR}} e^{-i\phi_{22}^{\text{NR}}}$. We compute the NR fluxes out of a certain sample of SXS datasets, and choose extrapolation order² $N = 4$ to avoid systematics during the inspiral.

¹ Along the z -axis orthogonal to the orbital plane. Since we are considering a nonprecessing system the components of the angular momentum along (x, y) directions are zero.

² For the time-domain phasing and unfaithfulness computations we use instead $N = 3$.

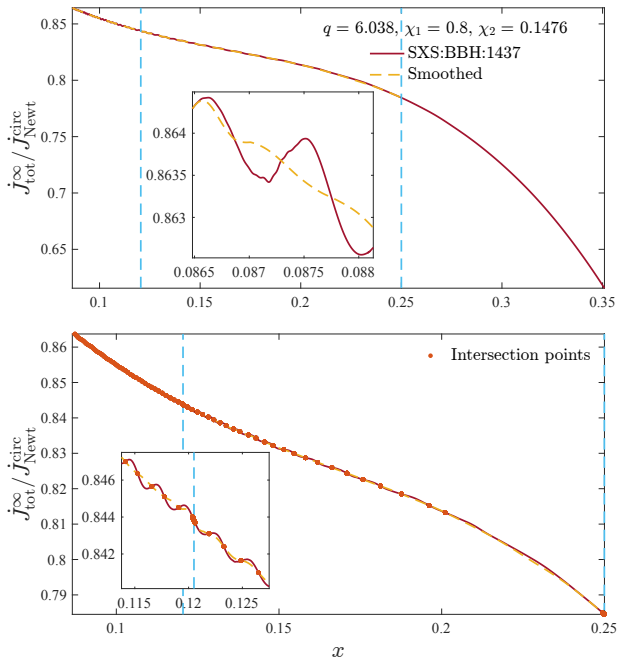


FIG. 1. Intermediate steps of the cleaning procedure. The x -domain is separated into three different parts, delimited by the vertical lines (top panel). No smoothing is applied on the third region, while the span of the moving average changes between the first and second region. The bottom panel focuses on the intersection points between the raw function and the smoothed one, that are finally fitted with a polynomial. The inset highlights the behavior around the interface between the first and second region.

When the so-computed fluxes are depicted in terms of the gauge-invariant frequency parameter

$$x_{\text{NR}} \equiv (\Omega_{\text{NR}})^{2/3} \quad (6)$$

one finds spurious oscillations. These oscillations are due to residual eccentricity (or other effects related to the BMS symmetry being violated [49]), and are additionally amplified when taking the derivatives. The amplification might be large and make the raw flux totally useless for any meaningful comparison with the analogous, fully nonoscillatory, EOB quantity. We have developed an efficient method to completely remove this oscillating behavior, and produce a rather clean and smooth representation of the flux versus x . The procedure is applied to the sample of SXS simulations reported in Table I, that is chosen so that the datasets distribution is approximately uniform over the NR-covered portion of the parameter space. We cut each flux at the NR merger, defined as the peak of $|h_{22}|$. The procedure uses a **MATLAB** function called `smooth`, i.e. a moving average whose span can be selected by the user³. The x -domain on which the flux

TABLE I. Sample of SXS spin-aligned datasets for which we compute the angular momentum flux. From left to right the columns display: the SXS ID; the binary parameters; the highest and second-highest level of resolution; the average of the difference between the raw flux and the cleaned one.

| ID | (q, χ_1, χ_2) | Lev _h | Lev _l | $\langle \Delta j_{\text{NR-NRclean}}^\infty \rangle$ |
|----------|------------------------|------------------|------------------|---|
| BBH:1155 | (1, 0, 0) | 3 | 2 | $1 \cdot 10^{-6}$ |
| BBH:1222 | (2, 0, 0) | 4 | 3 | $5.4 \cdot 10^{-5}$ |
| BBH:1179 | (3, 0, 0) | 5 | 4 | $1.8 \cdot 10^{-5}$ |
| BBH:0190 | (4.499, 0, 0) | 3 | 2 | $1.5 \cdot 10^{-5}$ |
| BBH:0192 | (6.58, 0, 0) | 3 | 2 | $1.3 \cdot 10^{-5}$ |
| BBH:1107 | (10, 0, 0) | 4 | 3 | $7.2 \cdot 10^{-5}$ |
| BBH:1137 | (1, -0.97, -0.97) | 4 | 2 | $6.3 \cdot 10^{-5}$ |
| BBH:2084 | (1, -0.90, 0) | 4 | 3 | $-2 \cdot 10^{-6}$ |
| BBH:2097 | (1, +0.30, 0) | 4 | 3 | $2.4 \cdot 10^{-5}$ |
| BBH:2105 | (1, +0.90, 0) | 4 | 3 | $2.3 \cdot 10^{-5}$ |
| BBH:1124 | (1, +0.99, +0.99) | 3 | - | $2.6 \cdot 10^{-5}$ |
| BBH:1146 | (1.5, +0.95, +0.95) | 2 | 0 | $1.2 \cdot 10^{-5}$ |
| BBH:2111 | (2, -0.60, +0.60) | 4 | 3 | $-9 \cdot 10^{-6}$ |
| BBH:2124 | (2, +0.30, 0) | 4 | 3 | $9 \cdot 10^{-6}$ |
| BBH:2131 | (2, +0.85, +0.85) | 4 | 3 | $2 \cdot 10^{-5}$ |
| BBH:2132 | (2, +0.87, 0) | 4 | 3 | $1.3 \cdot 10^{-5}$ |
| BBH:2133 | (3, -0.73, +0.85) | 4 | 3 | $2.2 \cdot 10^{-5}$ |
| BBH:2153 | (3, +0.30, 0) | 4 | 3 | $3.6 \cdot 10^{-5}$ |
| BBH:2162 | (3, +0.60, +0.40) | 4 | 3 | $1.7 \cdot 10^{-5}$ |
| BBH:1446 | (3.154, -0.80, +0.78) | 3 | 2 | $9 \cdot 10^{-6}$ |
| BBH:1936 | (4, -0.80, -0.80) | 3 | 2 | $-1.8 \cdot 10^{-5}$ |
| BBH:2040 | (4, -0.80, -0.40) | 3 | 2 | $7 \cdot 10^{-6}$ |
| BBH:1911 | (4, 0, -0.80) | 3 | 2 | $7 \cdot 10^{-6}$ |
| BBH:2014 | (4, +0.80, +0.40) | 3 | - | $-1 \cdot 10^{-6}$ |
| BBH:1434 | (4.368, +0.80, +0.80) | 3 | - | $2.5 \cdot 10^{-5}$ |
| BBH:1463 | (4.978, +0.61, +0.24) | 3 | 2 | $1.5 \cdot 10^{-5}$ |
| BBH:0208 | (5, -0.90, 0) | 3 | 2 | $9.2 \cdot 10^{-5}$ |
| BBH:1428 | (5.518, -0.80, -0.70) | 3 | 2 | $-2 \cdot 10^{-6}$ |
| BBH:1437 | (6.038, +0.80, +0.15) | 3 | 2 | $5 \cdot 10^{-6}$ |
| BBH:1436 | (6.281, +0.009, -0.80) | 3 | 2 | $1 \cdot 10^{-6}$ |
| BBH:1435 | (6.588, -0.79, +0.7) | 3 | 2 | $2 \cdot 10^{-6}$ |
| BBH:1448 | (6.944, -0.48, +0.52) | 3 | - | $2.1 \cdot 10^{-5}$ |
| BBH:1375 | (8, -0.90, 0) | 3 | - | $2.6 \cdot 10^{-5}$ |
| BBH:1419 | (8, -0.80, -0.80) | 3 | - | $-1.3 \cdot 10^{-5}$ |
| BBH:1420 | (8, -0.80, +0.80) | 3 | 2 | $2.2 \cdot 10^{-5}$ |
| BBH:1455 | (8, -0.40, 0) | 3 | 2 | $-3 \cdot 10^{-6}$ |

function is defined is separated into three parts: the first and the second ones get smoothed with different spans,

reciprocal of the span, meaning the higher the frequency of the oscillations to be removed, the higher the value of the chosen span.

³ Namely, it is a lowpass filter with filter coefficients equal to the

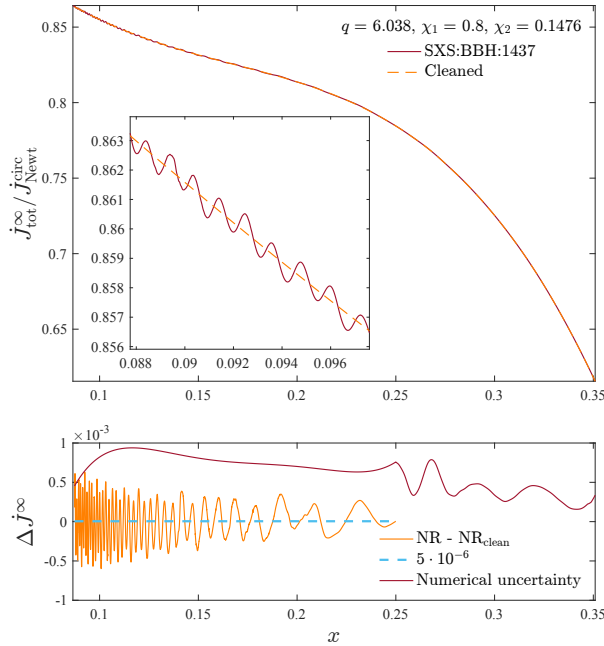


FIG. 2. The cleaned numerical angular momentum flux for the simulation SXS:BBH:1437 (dashed orange) is plotted against the original one (red). The inset in the upper panel shows how the final flux follows the original curve, averaging the oscillations. In the lower panel we display the difference between the cleaned and the raw flux, whose mean (dashed light blue line) is of order 10^{-5} , hence proving the effectiveness of the procedure. Our cleaning method also allows to estimate numerical accuracy (red curve), that is evaluated by subtracting to the cleaned flux its equivalent coming from the second-highest available resolution.

as the frequency of the oscillations progressively lowers; the third part, that is already essentially nonoscillatory, is left untouched. The three regions are optimized manually for each dataset in Table I. The cleaning procedure can be summarized in three steps: (i) we first apply the moving average to reduce the amplitude of the oscillations (see inset in the upper panel of Fig. 1); (ii) then we find the intersection points between the raw flux and the smoothed one, (see markers in the inset of Fig. 1); (iii) as a third step, the intersection points between the raw and the smoothed flux are fitted by a polynomial in x . For the datasets SXS:BBH:1155, SXS:BBH:1222, SXS:BBH:0190, SXS:BBH:0192 this is accomplished via a seventh order polynomial, while it suffices a fifth order one for the others⁴. The outcome of the fit is finally joined to the third part that was left unmodified. The final result, after some additional smoothing at the junction point, is shown in Fig. 2. Its reliability can be verified by computing the difference with the raw data and

checking that it averages zero. This is shown in the bottom panel of Fig. 2, where the residual does not show any evident global trend, actually averaging at $\sim 5 \times 10^{-6}$. To obtain a conservative estimate of the NR uncertainty on the final fluxes, we apply the cleaning procedure to both the highest and second highest available resolution and then take the difference. This is also shown in the bottom panel of Fig. 2. The procedure is found to be efficient and reliable for all configurations of Table I, where the quality of the cleaning procedure is indicated by the average of the difference between the raw flux and the cleaned one (last column of the table). The final result is displayed in Fig. 3. The figure highlights how both the value of the flux at merger and its global behavior have a clear dependence on the mass ratio and the effective Kerr parameter. This testifies how equal-mass binaries have a more adiabatic evolution, corresponding to slower plunges and a lower angular momentum loss. If the BHs have positive spins the plunge is even slower, owing to the well known effect of spin-orbit coupling (or hang-up effect) [7, 50]. Conversely for high mass ratio binaries (nearer to the test-mass limit) and negative spins, the fact that the system is progressively more and more non-adiabatic implies larger angular momentum losses, and the evolution ends at lower frequencies.

B. Angular momentum flux and radiation reaction within EOB

Let us now turn to discuss EOB fluxes within **TEOBResumS**. To do so, we start by reviewing the analytical elements of **TEOBResumS** that will be useful for our discussion. We use mass-reduced phase-space variables $(r, \varphi, p_\varphi, p_{r_*})$, related to the physical ones by $r = R/M$ (relative separation), $p_{r_*} = P_{R_*}/\mu$ (radial momentum), φ (orbital phase), $p_\varphi = P_\varphi/(\mu M)$ (angular momentum) and $t = T/M$ (time). The “tortoise” radial momentum is $p_{r_*} \equiv (A/B)^{1/2} p_r$, where A and B are the EOB potentials (with included spin-spin interactions [42]). The Hamilton’s equations for the relative dynamics read

$$\dot{\varphi} = \Omega = \partial_{p_\varphi} \hat{H}_{\text{EOB}}, \quad (7)$$

$$\dot{r} = \left(\frac{A}{B}\right)^{1/2} \partial_{p_{r_*}} \hat{H}_{\text{EOB}}, \quad (8)$$

$$\begin{aligned} \dot{p}_\varphi &= \hat{\mathcal{F}}_\varphi, \\ \dot{p}_{r_*} &= -\left(\frac{A}{B}\right)^{1/2} \partial_r \hat{H}_{\text{EOB}}, \end{aligned} \quad (9)$$

where \hat{H}_{EOB} is the EOB Hamiltonian [10], Ω is the orbital frequency and $\hat{\mathcal{F}}_\varphi$ is the radiation reaction force accounting for mechanical angular momentum losses due to GW emission. Note that within this context we are assuming that the radial force $\hat{\mathcal{F}}_r = 0$, that is equivalent to a gauge choice for circular orbits [5]. For a balance argument, the system angular momentum loss should be equal to the sum of the GW flux emitted at infinity, \dot{J}_∞ , and

⁴ Polynomials have been chosen after attempting different fitting functions, but they prove to be the simplest and more effective choice. We also found it more practical to apply a fit due to the large number of simulations taken into account.

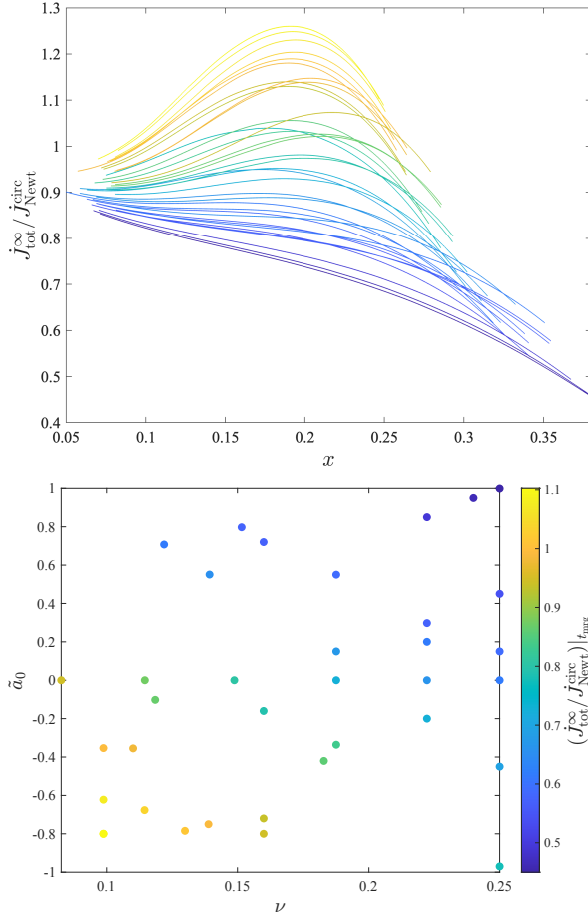


FIG. 3. The top panel shows the final outcome of the Newton-normalized angular momentum flux calculation for the NR datasets of Table I, with x given by Eq. (6), shown up to merger. The color code is chosen depending on the final value of the flux, displayed in the lower panel. The merger values show a clear dependence on ν and \tilde{a}_0 , mirroring whether the dynamics is more or less adiabatic: larger emissions correspond to faster plunges (with $\tilde{a}_0 < 0$).

absorbed by the event horizons of the two black holes, $\dot{J}_{H_{1,2}}$, that is

$$\dot{J}_{\text{system}} = \hat{\mathcal{F}}_\varphi = -\dot{J}_\infty - \dot{J}_{H_1} - \dot{J}_{H_2}. \quad (10)$$

In general, within this equation there should be an additional term accounting for Schott contributions, that are due to the interactions between the radiation and the field. However, it is always possible to choose a gauge such that there is no Schott contribution to the angular momentum [51] and this is the choice made here (on top of neglecting $\hat{\mathcal{F}}_r$). The azimuthal radiation reaction force is hence written as

$$\hat{\mathcal{F}}_\varphi = \hat{\mathcal{F}}_\varphi^\infty + \hat{\mathcal{F}}_\varphi^H, \quad (11)$$

where $\hat{\mathcal{F}}_\varphi^H$ is the horizon flux contribution [42]. The asymptotic term reads

$$\hat{\mathcal{F}}_\varphi^\infty = -\frac{32}{5}\nu r_\omega^4 \Omega^5 \hat{f}^\infty(v_\varphi^2; \nu), \quad (12)$$

where $\hat{f}^\infty(v_\varphi^2; \nu)$ is the reduced (i.e., Newton-normalized) flux function, $v_\varphi^2 \equiv (r_\omega \Omega)^2$ and r_ω is a modified radial separation defined in such a way that $1 = \Omega^2 r_\omega^3$ is valid during the plunge, fulfilling a modified Kepler's law that accounts for non-circularity [52, 53]. The reduced flux function is defined by normalizing the resummed circularized energy flux as $\hat{f} \equiv (\mathcal{F}_{22}^{\text{Newt}})^{-1} \sum \mathcal{F}_{\ell m}$, with all multipoles (except $m = 0$ modes) up to $\ell = 8$. The Newtonian term reads $\mathcal{F}_{22}^{\text{Newt}} = (32/5)\nu^2 x^5$ and the multipolar terms $\mathcal{F}_{\ell m}$ are factorized and resummed analogously to what is done for the waveform [54]. Explicitly, building upon Ref. [55], the structure of each flux multipole is

$$\mathcal{F}_{\ell m} = \mathcal{F}_{\ell m}^{\text{Newt}} |\hat{h}_{\ell m}|^2 \mathcal{F}_{\ell m}^{\text{NQC}}. \quad (13)$$

This is related to the correction entering the factorization of the waveform multipoles

$$h_{\ell m} = h_{\ell m}^{\text{Newt}} \hat{h}_{\ell m} \hat{h}_{\ell m}^{\text{NQC}} \quad (14)$$

where $h_{\ell m}^{\text{Newt}}$ is the Newtonian prefactor⁵, $\hat{h}_{\ell m}$ is the resummed PN correction and $\hat{h}_{\ell m}^{\text{NQC}}$ is the next-to-quasircular factor. The latter is described in more detail in Refs. [12, 42, 56, 57] (see in particular Sec. IIID of [12]). For each flux mode we have

$$\mathcal{F}_{\ell m}^{\text{NQC}} = \left| \hat{h}_{\ell m}^{\text{NQC}} \right|^2 = \left(1 + a_1^{\ell m} n_1^{\ell m} + a_2^{\ell m} n_2^{\ell m} \right)^2 \quad (15)$$

where $(n_1^{\ell m}, n_2^{\ell m})$ are functions of the radial momentum and of the radial acceleration (and a priori depend on the mode); $(a_1^{\ell m}, a_2^{\ell m})$ are numerical coefficients that are informed by NR simulations [42, 56] via an iterative procedure [58]. NQC corrections can, and actually should, be applied to each waveform (and thus flux) mode since they complete the analytical waveform, that is quasircular by construction. In practice, within **TEOBResumS** we add NQC corrections *only* in the $(2, 2)$ flux mode, while the waveform is NQC-completed up to $\ell = m = 5$ [12].

Finally, we remind that **TEOBResumS** is NR-informed via two different parameters, $a_6^c(\nu)$ and $c_3(\nu, \tilde{a}_1, \tilde{a}_2)$, respectively tuning the A potential and the spin-orbit sector of the model. Details on these functions can be found in Sec. IIC of Ref. [13].

For most of the analyses carried out in the following, we make use of the private **MATLAB** version of

⁵ As pointed out in Ref. [12], the standard Newtonian prefactors proportional to some power of v_φ are replaced in some multipoles by suitable powers of $v_\varphi v_\Omega$, with $v_\Omega = \Omega^{1/3}$. This is a practical solution to ease the action of the NR-informed NQC amplitude corrections and allow them to correctly capture the peak amplitude of each multipole. When including NQC corrections also in the higher mode contribution to the flux, this choice will eventually yield a partial inconsistency between the waveform and the flux. In Appendix B we show that by using the standard Newtonian prefactors in the waveform we generically improve the EOB/NR flux agreement for positive spins, but get inconsistent results for negative spins.

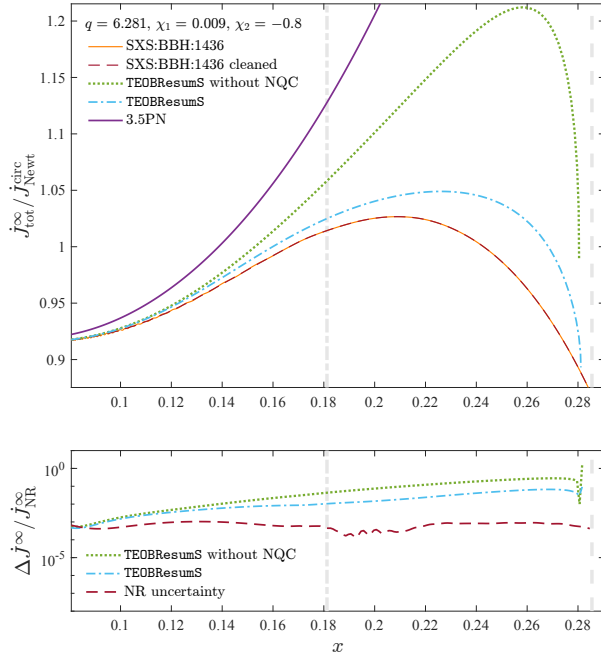


FIG. 4. Comparing Newton normalized total angular momentum fluxes summed up to $\ell_{\max} = 8$. The upper panel shows: (i) the raw numerical flux (orange) and as its cleaned version (dashed red); (ii) the EOB flux with $\ell = m = 2$ NQC corrections (dash-dotted light blue) and without (dotted green); (iii) the 3.5PN flux (purple). From left to right, the vertical lines indicate the EOB LSO and the NR merger respectively. Fractional differences are shown in the bottom panel, together with the NR uncertainty. NQC corrections are essential to reduce the gap between the EOB and NR curves.

TEOBResumS, in which we implement the changes for TEOBResumS_NQC_1m. The publicly available C version is used in the unfaithfulness calculation for the standard TEOBResumS.

C. Comparing NR and EOB fluxes

Let us now move to compare EOB and NR fluxes. The Newton-normalized EOB flux is expressed versus $x_{\text{EOB}} = \Omega^{2/3}$, while the NR curve is expressed versus $x_{\text{NR}} = \Omega_{\text{NR}}^{2/3}$ as defined above. To simplify the notation, in the figure we will simply use x for the horizontal axis, but it is intended that $x = x_{\text{NR}}$ when dealing with the NR curve and $x = x_{\text{EOB}}$ for the EOB curve. As an illustrative configuration we choose SXS:BBH:1436, corresponding to parameters $(q, \chi_1, \chi_2) = (6.281, 0.009, -0.8)$. The Newton-normalized, total, angular momentum flux, summed up to $\ell_{\max} = 8$ is displayed in Fig. 4. In particular, the figure shows: (i) the raw and cleaned NR fluxes, that are effectively indistinguishable on this scale; (ii) two EOB fluxes, one with the $\ell = m = 2$ NQC correction in the flux and another without it; (iii) the 3.5PN flux. The EOB fluxes prove both the power of resumma-

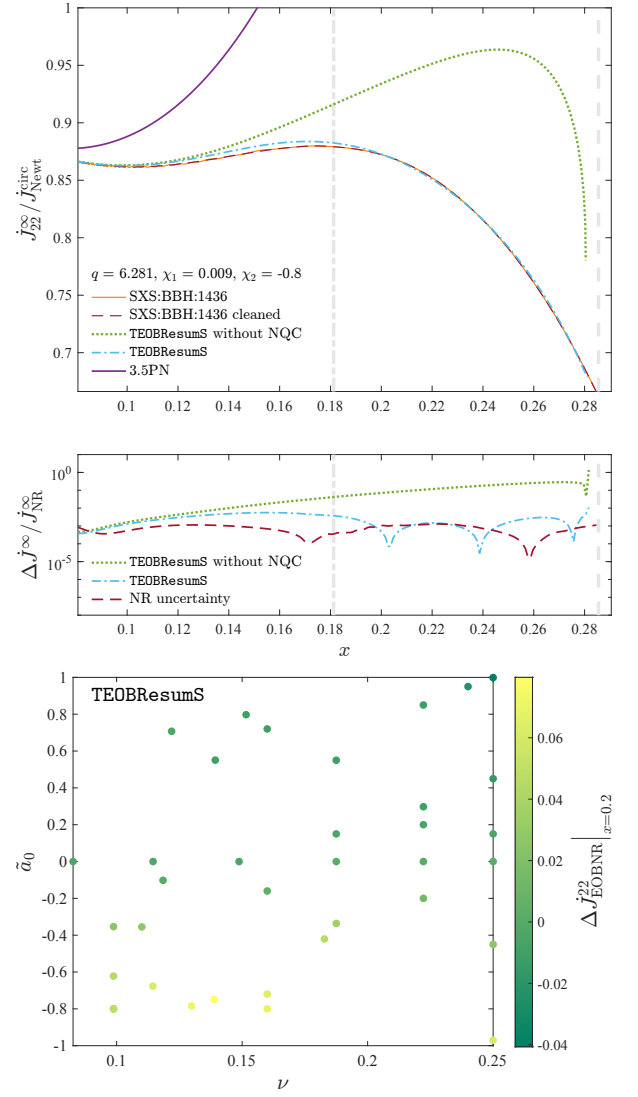


FIG. 5. *Top*: Comparing Newton-normalized $\ell = m = 2$ angular momentum fluxes, including again NR, the EOB fluxes with and without NQC corrections, and the 3.5PN result. Remarkably, the fractional difference with NR for the NQC-corrected EOB curve is of order 10^{-3} up to merger. The vertical lines indicate the LSO and the merger point. The $\ell = m = 2$ numerical flux has been cleaned separately from the total one, and the difference between the raw flux and the final fit averages to $-2 \cdot 10^{-5}$. *Bottom*: Fractional differences for the EOB/NR $\ell = m = 2$ fluxes at $x = 0.2$ for all configurations of Table I. The largest differences occur when $\tilde{a}_0 < 0$, where $x = 0.2$ approximately corresponds to the plunge regime.

tion techniques and the effectiveness of NQC corrections in achieving a good agreement with the NR quantities. The upper panel in Figure 5 is analogous to Fig. 4, but only focuses on the $\ell = m = 2$ contribution. The most interesting fact inferred by the plot is that the NQC factor is crucial to yield a fractional difference $\sim 10^{-3}$ up to merger. The lower panel of the same figure shows the distribution of the EOB/NR fractional difference at

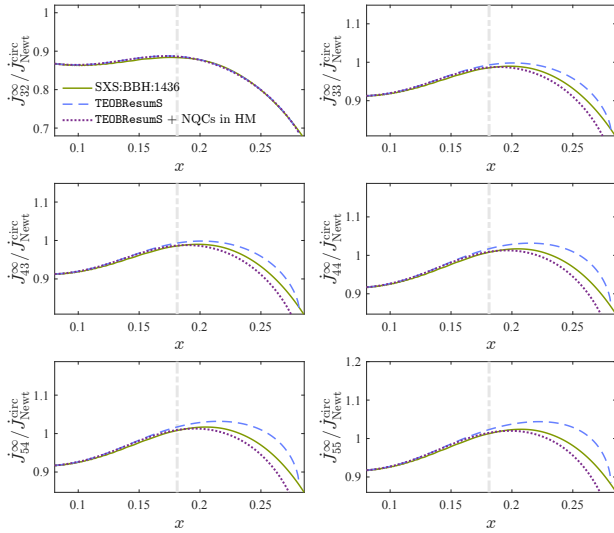


FIG. 6. Exploring the importance of higher modes using the SXS:BBH:1436 dataset. In each panel the flux is summed up to the indicated (ℓ, m) mode. NQC corrections are included either in the $\ell = m = 2$ EOB mode only (dashed blue line) or in all $\ell = m$ modes up to $\ell = 5$ (dotted purple line). The NR-informed NQC corrections in higher modes are essential to improve the EOB/NR agreement beyond plunge (the vertical line indicates the LSO frequency) and up to merger.

$x = 0.2$ over the parameter space. This seems to point out to a decreased agreement for configurations having a negative \tilde{a}_0 , but one has to note however that, as can be seen in Fig. 3, the fluxes for these datasets end at lower frequencies and hence $x = 0.2$ corresponds to the late plunge.

The cumulative importance of higher modes with respect to the $\ell = m = 2$ one is studied in Fig. 6 for the same SXS:BBH:1436 configuration. The figure contrasts the EOB flux with the NR one, where both functions incorporate modes summed up to the indicated (ℓ, m) value. The plot shows that for the standard **TEOBResumS** the EOB/NR agreement progressively worsens during the late inspiral up to merger, due to the lack of the NR-informed NQC corrections beyond the $\ell = m = 2$ ones. Including NQC corrections in the flux in all the $\ell = m$ modes up to $\ell = 5$ yields a closer agreement between the analytical and numerical fluxes up to merger. The NQC parameters are determined with the usual iteration procedure, although we maintain the same values of the NR-informed parameters (a_6^5, c_3) determined with the standard $\ell = m = 2$ NQC correction. The effect is very evident for this specific dataset, but it is a feature that is always present, also for other configurations. This exercise indicates that to increase the physical completeness and NR-consistency of **TEOBResumS** it would be needed to include NQC corrections *at least* in the $\ell = m$ multipoles in the flux. Evidently, this operation will eventually imply the need of constructing new NR-informed (a_6^5, c_3) functions that are consistent

TABLE II. Binary configurations, first-guess values of c_3 used to inform the global interpolating fit given in Eq. (22), and the corresponding c_3^{fit} values.

| # | ID | (q, χ_1, χ_2) | \tilde{a}_0 | $c_3^{\text{first guess}}$ | c_3^{fit} |
|----|----------|--------------------------|---------------|----------------------------|--------------------|
| 1 | BBH:1137 | (1, -0.97, -0.97) | -0.97 | 89.7 | 89.33 |
| 2 | BBH:0156 | (1, -0.9498, -0.9498) | -0.95 | 88.5 | 88.33 |
| 3 | BBH:0159 | (1, -0.90, -0.90) | -0.90 | 84.5 | 85.86 |
| 4 | BBH:2086 | (1, -0.80, -0.80) | -0.80 | 82 | 80.93 |
| 5 | BBH:2089 | (1, -0.60, -0.60) | -0.60 | 71 | 71.19 |
| 6 | BBH:0150 | (1, +0.20, +0.20) | +0.20 | 35.5 | 35.73 |
| 7 | BBH:2102 | (1, +0.60, +0.60) | +0.60 | 22.2 | 21.67 |
| 8 | BBH:2104 | (1, +0.80, +0.80) | +0.80 | 15.9 | 16.31 |
| 9 | BBH:0153 | (1, +0.85, +0.85) | +0.85 | 15.05 | 15.29 |
| 10 | BBH:0160 | (1, +0.90, +0.90) | +0.90 | 14.7 | 14.5 |
| 11 | BBH:0157 | (1, +0.95, +0.95) | +0.95 | 14.3 | 14.1 |
| 12 | BBH:0177 | (1, +0.99, +0.99) | +0.99 | 14.2 | 14.29 |
| 13 | BBH:0004 | (1, -0.50, 0.0) | -0.25 | 55.5 | 54.44 |
| 14 | BBH:0005 | (1, +0.50, 0.0) | +0.25 | 35 | 34.17 |
| 15 | BBH:2105 | (1, +0.90, 0.0) | +0.45 | 27.7 | 27.21 |
| 16 | BBH:2106 | (1, +0.90, +0.50) | +0.70 | 19.1 | 19.09 |
| 17 | BBH:0016 | (1.5, -0.50, 0.0) | -0.30 | 56.2 | 56.14 |
| 18 | BBH:1146 | (1.5, +0.95, +0.95) | +0.95 | 14.35 | 13.98 |
| 19 | BBH:2129 | (2, +0.60, 0.0) | +0.40 | 29.5 | 29.31 |
| 20 | BBH:2130 | (2, +0.60, +0.60) | +0.60 | 23 | 22.41 |
| 21 | BBH:2131 | (2, +0.85, +0.85) | +0.85 | 16.2 | 15.73 |
| 22 | BBH:2139 | (3, -0.50, -0.50) | -0.50 | 65.3 | 62.45 |
| 23 | BBH:0036 | (3, -0.50, 0.0) | -0.38 | 58.3 | 57.62 |
| 24 | BBH:0174 | (3, +0.50, 0.0) | +0.37 | 28.5 | 30.87 |
| 25 | BBH:2158 | (3, +0.50, +0.50) | +0.50 | 27.1 | 26.64 |
| 26 | BBH:2163 | (3, +0.60, +0.60) | +0.60 | 24.3 | 23.56 |
| 27 | BBH:0293 | (3, +0.85, +0.85) | +0.85 | 17.1 | 17.05 |
| 28 | BBH:1447 | (3.16, +0.7398, +0.80) | +0.75 | 19.2 | 19.46 |
| 29 | BBH:2014 | (4, +0.80, +0.40) | +0.72 | 21.5 | 21.52 |
| 30 | BBH:1434 | (4.37, +0.7977, +0.7959) | +0.80 | 19.8 | 20.05 |
| 31 | BBH:0111 | (5, -0.50, 0.0) | -0.42 | 54 | 57.18 |
| 32 | BBH:0110 | (5, +0.50, 0.0) | +0.42 | 32 | 30.98 |
| 33 | BBH:1432 | (5.84, +0.6577, +0.793) | +0.68 | 25 | 24.42 |
| 34 | BBH:1375 | (8, -0.90, 0.0) | -0.80 | 64.5 | 65.12 |
| 35 | BBH:0114 | (8, -0.50, 0.0) | -0.44 | 57 | 56.07 |
| 36 | BBH:0065 | (8, +0.50, 0.0) | +0.44 | 29.5 | 31.78 |
| 37 | BBH:1426 | (8, +0.4838, +0.7484) | +0.51 | 30.3 | 29.98 |

with the new choice of radiation reaction⁶.

⁶ Note that part of the residual difference cannot be totally removed because the Newtonian prefactors in the waveform are not consistent with those in the flux for $\ell = m > 2$, as pointed out above. See Appendix B for other details.

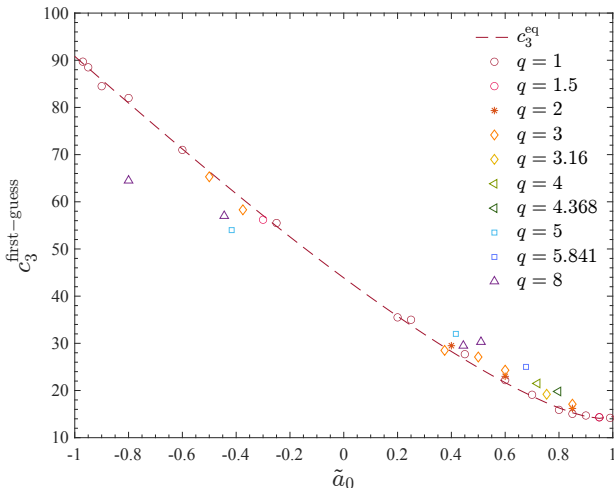


FIG. 7. The first-guess c_3 values of Table II versus the spin variable \tilde{a}_0 . The unequal-spin and unequal-mass points can be essentially seen as a correction to the equal-mass, equal-spin values. The latter are fitted to obtain the first part of the fit, c_3^{eq} (dashed red).

III. IMPROVING THE CONSISTENCY BETWEEN WAVEFORM AND FLUX OF TEOBRESUMS

Let us construct a modified TEOBResumS model that incorporates iterated NQC corrections in all $\ell = m$ modes in the flux up to $\ell = 5$. Since we are modifying the radiation reaction, this choice in principle calls for a new determination of both the a_6^c and c_3 functions. However, we have verified that the improvements brought by a newly tuned $a_6^c(\nu)$ are marginal, so that, for the sake of simplicity, we keep its standard expression that we quote here for completeness as

$$a_6^c = n_0 \frac{1 + n_1\nu + n_2\nu^2 + n_3\nu^3}{1 + d_1\nu}, \quad (16)$$

where

$$n_0 = 5.9951, \quad (17)$$

$$n_1 = -34.4844, \quad (18)$$

$$n_2 = -79.2997, \quad (19)$$

$$n_3 = 713.4451, \quad (20)$$

$$d_1 = -3.167. \quad (21)$$

By contrast, we look for a new NR-informed representation of c_3 . We follow our usual procedure, that is described for example in Sec. IIB.2 of Ref. [10]. Typically, for each NR dataset one determines a value of c_3 so that the EOB/NR accumulated phase difference up to merger is within (or compatible with) the NR phase uncertainty at NR merger. This leaves a certain flexibility and arbitrariness in the choice of c_3 and, in previous attempts, we were typically accepting EOB/NR phase differences

of the order of 0.1-0.2 rad at merger. Here, on the understanding that the NR phase uncertainty might be overestimated by taking the difference between the two highest resolutions, we attempt to ask more, requiring that the EOB/NR phase difference is *as flat as possible* through inspiral, merger and ringdown when the two waveforms are aligned during the early inspiral. As a cross check, we also align the two waveforms during the late plunge, just before merger, to verify that the phase difference keeps remaining flat. This further proves that the c_3 determination, that mostly affects the plunge phase, is done robustly. To exploit at best current NR information, we consider a sample of 37 SXS configurations, most of which were already taken into account in the previous determinations of c_3 . Here we replaced some datasets used in Ref. [10] with newer ones with improved accuracy and included a few more simulations so as to cover the parameter space more efficiently. Table II reports the SXS configurations, the corresponding values of \tilde{a}_0 , the first-guess values of c_3 obtained with the procedure explained above as well as the corresponding ones obtained after a global fit. Specifically, the $c_3^{\text{first-guess}}$ data of Table II are fitted with a global function as $c_3(\nu, \tilde{a}_0, \tilde{a}_{12})$ that reads

$$c_3(\nu, \tilde{a}_0, \tilde{a}_{12}) = p_0 \frac{1 + n_1\tilde{a}_0 + n_2\tilde{a}_0^2 + n_3\tilde{a}_0^3 + n_4\tilde{a}_0^4}{1 + d_1\tilde{a}_0} + p_1\tilde{a}_0\sqrt{1 - 4\nu} + p_2\tilde{a}_0^2\sqrt{1 - 4\nu} + p_3\tilde{a}_0\nu\sqrt{1 - 4\nu} + p_4\tilde{a}_{12}\nu^2, \quad (22)$$

where the fitted parameters are

$$p_0 = 43.872788, \quad (23)$$

$$n_1 = -1.849495, \quad (24)$$

$$n_2 = 1.011208, \quad (25)$$

$$n_3 = -0.086453, \quad (26)$$

$$n_4 = -0.038378, \quad (27)$$

$$d_1 = -0.888154, \quad (28)$$

$$p_1 = 26.553, \quad (29)$$

$$p_2 = -8.65836, \quad (30)$$

$$p_3 = -84.7473, \quad (31)$$

$$p_4 = 24.0418. \quad (32)$$

Figure 7 highlights that the span of the “best” (first-guess) values of c_3 is rather limited (especially for spins aligned with the orbital angular momentum) around the equal-mass, equal-spin case. As in previous work, the fitting procedure consists of two steps. First, one fits the equal-mass, equal-spin data with a quasi-linear function of $\tilde{a}_0 = \tilde{a}_1 + \tilde{a}_2$ with $\tilde{a}_1 = \tilde{a}_2$. This delivers the six parameters $(p_0, n_1, n_2, n_3, n_4, d_1)$. The corresponding fit c_3^{eq} is shown as a dashed red curve in Fig. 7. Note that the analytical structure of the fitting function was chosen in order to accurately capture the nonlinear behavior of c_3 for $\tilde{a}_0 \rightarrow 1$. In the second step one subtracts this fit from the corresponding $c_3^{\text{first-guess}}$ values and fits the

residual. This determines the parameters (p_1, p_2, p_3, p_4) . The novelty with respect to previous work is that the functional form chosen for the unequal-mass, unequal-spin fit is more effective in capturing the first-guess values all over the SXS sample considered.

To give a flavor of the improved EOB/NR agreement that can be obtained with the new c_3 and with the new radiation reaction, let us report a few examples. From now on we will refer to the improved model as `TEOBResumS_NQC_1m`, to easily distinguish it from `TEOBResumS`. Figure 8 shows the updated flux comparison for SXS:BBH:1436, and also includes the dataset SXS:BBH:1437 with $(q, \chi_1, \chi_2) = (6.038, 0.8, 0.1476)$. The addition of NQC corrections to $\ell = m$ modes up to $\ell = 5$ of the radiation reaction is essential to improve the behavior of the analytic flux towards merger. For `TEOBResumS_NQC_1m` the fractional difference between EOB/NR total fluxes for the configuration SXS:BBH:1436 remains below 10^{-2} until $x \sim 0.26$. By contrast, in Fig. 4, the fractional difference for `TEOBResumS` already reached 10^{-2} at the LSO and kept growing until merger.

We finally test the performance of the model over all datasets of Table I, by computing the fractional difference between EOB and NR (total) fluxes at $x = 0.2$ for both `TEOBResumS` and `TEOBResumS_NQC_1m`, as shown respectively in the top and bottom panel of Fig. 9. Here one can see an evident improvement for larger mass ratios and negative values of the effective Kerr parameter.

Another example is shown in Fig. 10, that focuses on time-domain phasings. We use here the Regge-Wheeler-Zerilli normalized waveform, defined as $\Psi_{\ell m} = h_{\ell m} / \sqrt{(\ell-1)\ell(\ell+1)(\ell+2)}$. The EOB waveforms have been obtained by setting the spin values with 6 digits precision, considering the initial χ_1, χ_2 given in the metadata file for each simulation⁷. The figure contrasts EOB/NR waveform phasings for the $\ell = m = 2$ multipole, considering datasets SXS:BBH:1463 (first row) and SXS:BBH:1426 (second row) using `TEOBResumS` (left) and `TEOBResumS_NQC_1m` (right). As usually done, in this case we are using $N = 3$ extrapolation order for the SXS waveforms. In each figure, the top panels show the phase and amplitude difference, where $\Delta\phi_{22}^{\text{EOBNR}} \equiv \phi_{22}^{\text{EOB}} - \phi_{22}^{\text{NR}}$. The EOB/NR phasing agreement is better for `TEOBResumS_NQC_1m` than for `TEOBResumS`, although the SXS:BBH:1426 dataset is among those used to inform the new expression of c_3 .

IV. EOB/NR $\ell = m = 2$ UNFAITHFULNESS

A global view of the EOB/NR agreement is given by the computation of the EOB/NR unfaithfulness as a

function of the total mass of the system. As done for the time-domain phasing, for the EOB spin values we take the initial (χ_1, χ_2) given in the metadata file for each simulation with 6 digits precision. For simplicity, here we focus only on the $\ell = m = 2$ mode. Considering two waveforms (h_1, h_2) with same fixed mass ratio and spins, the unfaithfulness is a function of the total mass M of the binary and is defined as

$$\bar{F}(M) \equiv 1 - F = 1 - \max_{t_0, \phi_0} \frac{\langle h_1, h_2 \rangle}{\|h_1\| \|h_2\|}, \quad (33)$$

where (t_0, ϕ_0) are the initial time and phase, $\|h\| \equiv \sqrt{\langle h, h \rangle}$, and the inner product between two waveforms is defined as $\langle h_1, h_2 \rangle \equiv 4\Re \int_{f_{\min}^{\text{NR}}(M)}^{\infty} \tilde{h}_1(f) \tilde{h}_2^*(f) / S_n(f) df$, where $\tilde{h}(f)$ denotes the Fourier transform of $h(t)$, $S_n(f)$ is the detector's power spectral density (PSD) and $f_{\min}^{\text{NR}}(M) = \hat{f}_{\min}^{\text{NR}}/M$ is the initial frequency of the NR waveform. In practice, the integral is done up to a maximal NR frequency f_{\max}^{NR} that is chosen as the frequency where the amplitude of \tilde{h}_{NR} is 10^{-3} . Waveforms are tapered in the time-domain at the beginning of the inspiral so as to reduce the presence of high-frequency oscillations in the corresponding Fourier transforms. As a step forward to previous work, we here consider for this calculation not only the standard zero-detuned, high-power noise spectral density of Advanced LIGO [43], but also the anticipated PSD of Einstein Telescope, considering its latest sensitivity model ET-D [45], and of Cosmic Explorer [46]. The corresponding PSDs are shown in Fig. 11, together with the less recent ET-C version of the PSD of Einstein Telescope [44]. As a complementary analysis we perform the unfaithfulness computation for this PSD in Appendix C.

The outcome of the $\bar{F}(M)$ computation is shown in Fig. 12, where we used Eq. (33) with $h_1 = h_{\text{EOB}}$ and $h_2 = h_{\text{NR}}$. For each detector choice, the top panels of the figure displays the results obtained with `TEOBResumS`, while the bottom ones those pertaining to `TEOBResumS_NQC_1m`. For what concerns the aLIGO PSD, the first column of Fig. 12 highlights that $\bar{F}_{\text{EOB/NR}}^{\text{max}}$ comfortably stays well below the 10^{-2} threshold, all over the parameter space. More precisely, one finds that for `TEOBResumS_NQC_1m` the datasets in the range $10^{-3} < \bar{F}_{\text{EOB/NR}}^{\text{max}} < 10^{-2}$ are 18.4% (see Table III), out of which 1.7% have a maximum $\bar{F}_{\text{EOB/NR}}$ value above 3×10^{-3} , where the latter percentage value is lower than the one related to `TEOBResumS`. The largest unfaithfulness values obtained with `TEOBResumS_NQC_1m`, $\bar{F}_{\text{EOB/NR}}^{\text{max}} = (0.47, 0.49)\%$, correspond respectively to the extremely spinning configuration SXS:BBH:1124 with $(1, +0.998, +0.998)$ and to the configuration SXS:BBH:1434 with $(4.367, +0.798, +0.795)$. In general, as deducible from Fig. 14, the largest values of $\bar{F}_{\text{EOB/NR}}^{\text{max}}$ are obtained for the datasets with individual spins large and positive, i.e. in a regime where we a priori expect the largest uncertainties in both the NR waveforms and

⁷ We noticed a decreased phase difference at merger when using larger precisions.

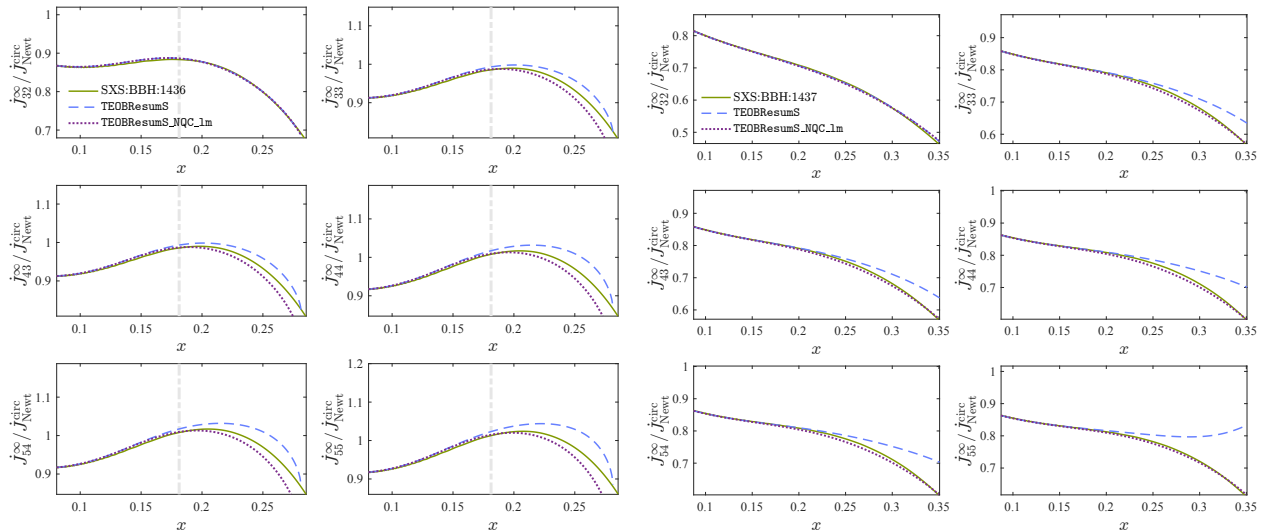


FIG. 8. *Left:* Analogous of Fig. 6 obtained using the new model, showing that the change in c_3 does not affect the behavior of the flux. When summing up to $\ell = 8$ as done in Fig. 4, the EOB/NR fractional difference for **TEObResumS_NQC_1m** remains below 10^{-2} for most of the evolution, even beyond the LSO. *Right:* Contrasting the performance of **TEObResumS** and **TEObResumS_NQC_1m** for the dataset SXS:BBH:1437 with $(q, \chi_1, \chi_2) = (6.038, 0.8, 0.1476)$. The behavior of the flux up to $\ell = 8$ progressively gets less robust and is discussed in Appendix A.

in the model. Our result already represents nonnegligible quantitative progress with respect to Refs. [13, 57]. Still, there exists room for improvement, since the NR error is estimated between 10^{-6} and 10^{-4} , as shown in the right panel of Fig. 2 of Ref. [13].

For what concerns ET-D, the second column of Fig. 12 and Table III highlight that $\bar{F}_{\text{EOB/NR}}^{\text{max}}$ mostly stays below 10^{-3} . For **TEObResumS_NQC_1m**, there are only 11 configurations with $\bar{F}_{\text{EOB/NR}}^{\text{max}} > 3 \times 10^{-3}$, and again the highest values correspond to SXS:BBH:1124 and SXS:BBH:1434. Moreover, 79.9% of the total number of mismatches for **TEObResumS_NQC_1m** are in the range $10^{-4} < \bar{F}_{\text{EOB/NR}} < 10^{-3}$ and 3.9% of the total mismatches are below 10^{-4} (see Table III).

Finally, regarding CE, only 1.3% of the configurations have $\bar{F}_{\text{EOB/NR}}^{\text{max}} > 3 \cdot 10^{-3}$, and the percentage of those below 10^{-3} reaches 84.1%. It is quite remarkable that for this detector 6.4% of the total mismatches using **TEObResumS_NQC_1m** are below 10^{-4} .

Concerning the two configurations displayed in Fig. 10, the lowered phase difference at merger for **TEObResumS_NQC_1m** reflects in a slightly lower value of $\bar{F}_{\text{EOB/NR}}^{\text{max}}$. Namely, for the dataset SXS:BBH:1463, the [%] unfaithfulness switches from (0.1437, 0.1736, 0.1323) respectively for aLIGO, ET-D and CE to (0.1434, 0.1703, 0.1323), while for the dataset SXS:BBH:1426, the values lower from (0.1671, 0.1985, 0.1546) to (0.0675, 0.0731, 0.0613).

Figures 12, 13 and 14 represent, to our knowledge, the first systematic assessment of the quality of a state-of-the-art waveform model in view of the 3G detector effort [36–41]. Our plots look a bit more optimistic than the conclusions of Ref. [59], that assessed the quality of

the phenomenological waveform model **IMRPhenomPv2** for specific configurations, and concluded that the accuracy of current waveform models needs to be improved by at least three orders of magnitude. If this is certainly true of **IMRPhenomPv2**, it doesn't seem to be the case for the spin-aligned model that we are discussing here, as it already grazes the expected detector calibration uncertainty, $\sim 10^{-5}$, for masses up to $20M_{\odot}$. For larger values of M , where the detector is mostly sensitive to the ringdown, $\bar{F}_{\text{EOB/NR}}$ goes up to 10^{-3} for several configurations. This however should be carefully interpreted, since it is related to two physical facts: (i) on the one hand, the quality of the late part of the NR ringdown might be more or less noisy depending on the configuration, thus affecting the unfaithfulness calculation; (ii) on the other hand, even if there was no relevant numerical noise, there are differences between the EOB modeled ringdown and the actual one. In particular, the absence of mode mixing between positive and negative frequency QNMs (a phenomenon that is present especially for spins anti-aligned with the angular momentum) can play a role in this context. In addition, one should also be aware of the fact that the NR-informed postmerger was constructed using SXS data extrapolated with $N = 2$ [13], since this reduces the amount of NR noise during this specific part of the waveform. However, the EOB/NR comparison is done using $(N = 3)$ -extrapolated waveform data, that gives a good compromise between the inspiral and the merger-ringdown part of the signal. This means that the differences that we see in Fig. 12 for large masses are *partly* coming from the NR simulations and not from the model. We thus expect that our EOB/NR comparisons will benefit of improved NR simulations that use Cauchy

TABLE III. Quantifying the EOB/NR agreement. The central columns of the table contain the fraction of datasets whose maximum unfaithfulness $\bar{F}_{\text{EOB/NR}}^{\text{max}}$ is within the indicated limits for either **TEOBResumS** or **TEOBResumS_NQC_1m**. The last two columns display percentage numbers out of *all* the mismatch values. These are found independently of the single simulations, by considering how many points pertaining to the curves of Fig. 12 fall into a certain range of \bar{F} . The range in M is $2.5M_{\odot}$.

| | | $\bar{F}^{\text{max}} < 10^{-3}$ | $10^{-3} < \bar{F}^{\text{max}} < 10^{-2}$ | $\bar{F}^{\text{max}} > 3 \times 10^{-3}$ | $10^{-4} < \bar{F} < 10^{-3}$ | $\bar{F} < 10^{-4}$ |
|-------|--------------------------|----------------------------------|--|---|-------------------------------|---------------------|
| aLIGO | TEOBResumS | 83.1% | 16.9% | 2.1% | 83.9% | 3.1% |
| | TEOBResumS_NQC_1m | 82.0% | 18.4% | 1.7% | 81.5% | 3.8% |
| ET-D | TEOBResumS | 83.5% | 15.9% | 2.6% | 82.9% | 3.2% |
| | TEOBResumS_NQC_1m | 81.5% | 18.5% | 2.1% | 79.9% | 3.9% |
| CE | TEOBResumS | 85.6% | 14.8% | 1.7% | 84.7% | 5.2% |
| | TEOBResumS_NQC_1m | 84.1% | 16.7% | 1.3% | 82.8% | 6.4% |

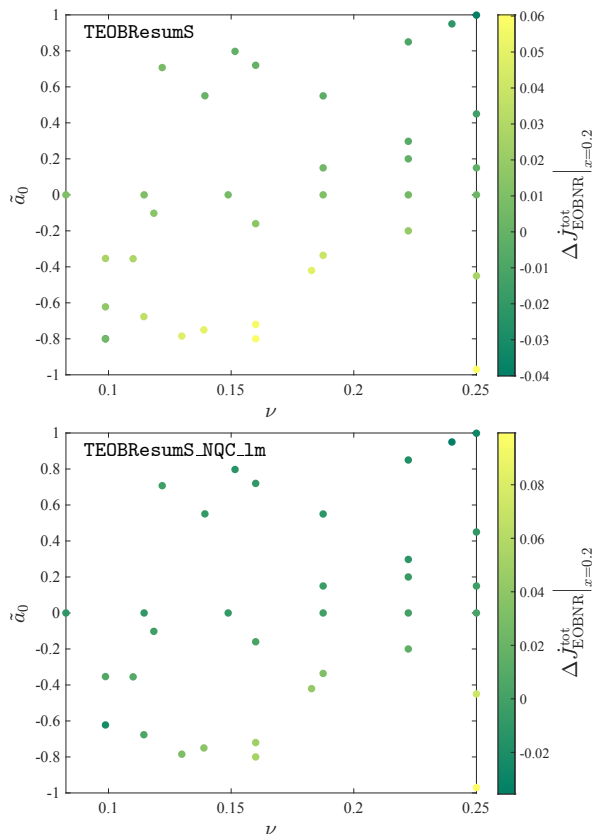


FIG. 9. Fractional EOB/NR flux differences at $x = 0.2$ for **TEOBResumS** (top) and **TEOBResumS_NQC_1m** (bottom) evaluated for the sample of SXS data of Table I. For **TEOBResumS_NQC_1m** we are excluding from the points two configurations, corresponding to datasets SXS:BBH:1419 and SXS:BBH:1375, where the contribution of modes with $\ell_{\text{max}} > 5$ becomes important towards merger. These will be discussed in Appendix A.

Characteristic Extraction [60–62].

On a more general ground, a precise assessment of the accuracy of the current version(s) of **TEOBResumS** for ET will require dedicated injection/recovery campaigns.

Nonetheless our analysis seems to indicate that both versions of **TEOBResumS**, either the standard or the NQC-improved one, already offer a reliable starting point to investigate PE having in mind 3G detectors. To obtain such result it was crucial to improve the self-consistency of the model and to provide a new analytical representation of the c_3 function carefully selecting a new sample of useful NR datasets.

V. CONTRASTING TEOBRESUMS AND SEOBNRV4HM WAVEFORM MODELS

Now that we have explored the performance of **TEOBResumS** under a different point of view and shown how to improve it further, let us shift to compare it with **SEOBNRv4HM** [14, 47, 48]. This model is another state-of-the-art EOB model informed by NR simulations and differs from **TEOBResumS** for several structural choices, that involve the structure of the Hamiltonian, the gauge, the analytic content and the resummation strategies. A comprehensive analysis of what distinguishes the Hamiltonians of **TEOBResumS** and of **SEOBNRv4HM** is presented in Ref. [27]. The **SEOBNRv4** model was presented in 2016 and never structurally updated since, except for the addition of higher modes [48], without any change to the dynamics, and precession [14]. The purpose of this section is to discuss more specific comparisons between the two models, especially focusing on frequencies and angular momentum fluxes. Moreover, even if **TEOBResumS** has been publicly available for many years [10], direct comparisons involving both EOB models and the full NR catalog do not seem to exist in the literature. Note however that **SEOBNRv4HM** was compared to the most recent generation of phenomenological models (see in particular Fig.17 of Ref. [22]). We aim at filling this gap by providing one-to-one comparisons between **SEOBNRv4HM** and **TEOBResumS** that involve the important observables discussed so far: (i) angular momentum fluxes; (ii) waveform amplitude and frequency and the consistency of this latter with the dynamics; (iii) EOB/NR unfaithful-

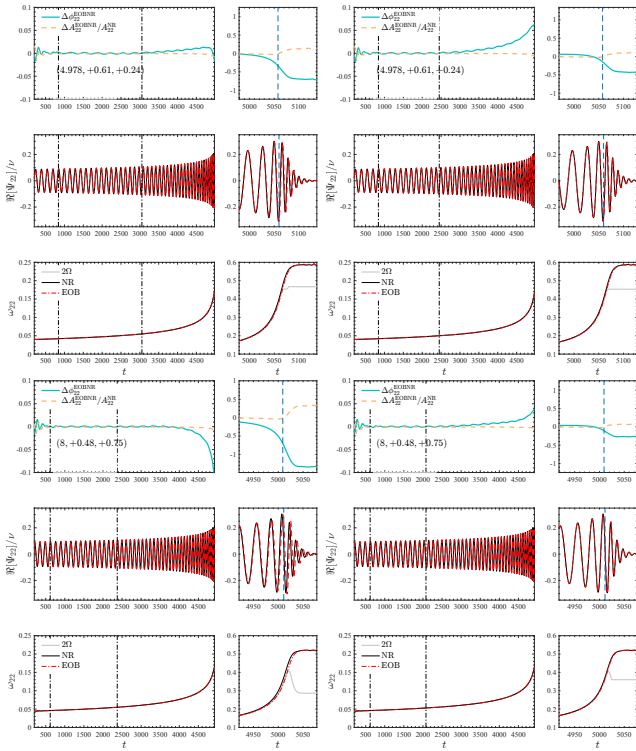


FIG. 10. EOB/NR time-domain phasing for two illustrative datasets: SXS:BBH:1463 with $(q, \chi_1, \chi_2) = (4.978, +0.61, +0.24)$ (top panels) and SXS:BBH:1426 with $(q, \chi_1, \chi_2) = (8, +0.48, +0.75)$ (bottom panels), using **TEOBResumS** (left) and **TEOBResumS_NQC_1m** (right). Each plot shows: (i) the phase difference and the relative amplitude difference; (ii) the real parts of the EOB and NR waveforms; (iii) the instantaneous GW frequency together with twice the orbital frequency Ω . Vertical dash-dotted lines indicate the alignment interval. The phase differences $\Delta\phi_{22}^{\text{EOBNR}}$ at merger (vertical dashed blue line) are respectively $(-0.34, -0.70)$ rad for **TEOBResumS** and become $(-0.14, -0.11)$ for **TEOBResumS_NQC_1m**. Note that only SXS:BBH:1426 was used to inform c_3 .

ness computations taking into account also 3G detectors. In this section we will use *only* the standard version of **TEOBResumS**. In addition, for the unfaithfulness calculation we will use the publicly available *C* implementation⁸, that employs fits for the $\ell = m = 2$ NQC parameters entering the flux as well as the (iterated) post-adiabatic approximation [9] to efficiently describe the inspiral, as detailed in Ref. [57].

A. Angular momentum fluxes

Let us firstly discuss the flux of angular momentum. To begin with, one has to be aware that – to the best of

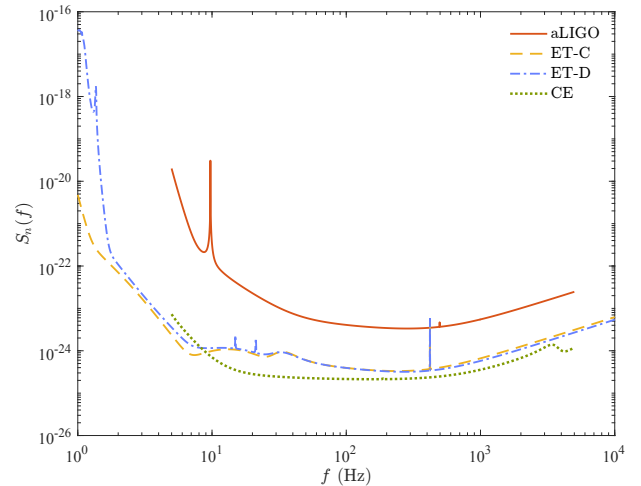


FIG. 11. Sensitivity curves for the three detectors we take into consideration in computing the unfaithfulness for the two versions of our model: Advanced LIGO, Einstein Telescope (ET) and Cosmic Explorer (CE). Here ET-C is the sensitivity model described in Ref. [44], while ET-D is the latest version [45].

our knowledge – the dynamical phase-space variables are not among the standard outputs of the **SEOBNRv4HM** implementation within **LALSimulation**, so that some modifications of the code are needed⁹. This was done and explicitly described already in Ref. [12]. The simplest way to compute the angular momentum flux for **SEOBNRv4HM** is by taking the time derivative of the angular momentum p_φ , i.e. using the relation

$$\dot{J}_{\text{SEOB}} = -\dot{p}_\varphi^{\text{SEOB}} = -\dot{\mathcal{F}}_\varphi^{\text{SEOB}}. \quad (34)$$

Figure 15 displays the related fluxes for the configurations $(1.5, 0.95, 0.95)$, $(2, 0.85, 0.85)$, $(2, -0.6, 0.6)$ and $(5.52, -0.8, -0.7)$, corresponding to SXS datasets SXS:BBH:1146, SXS:BBH:2131, SXS:BBH:2111 and SXS:BBH:1428. Each panel compares five curves: (i) the NR flux (red); (ii) the standard **TEOBResumS** flux; (iii) the flux from **TEOBResumS** without the $\ell = m = 2$ NQC corrections; (iv) the **SEOBNRv4HM** flux. Let us firstly focus on the two cases with the largest spins, top row of Fig. 15: the figure highlights the differences between the **SEOBNRv4HM** and NR fluxes. We believe this is related to the **SEOBNRv4HM** dynamics for these two configurations, as we will further point out in Sec. VB below. By contrast, the **TEOBResumS** fluxes look consistent with the NR one. In particular, the agreement that can be reached between **TEOBResumS** and NR *without* the NQC correction factor is remarkable. However, this also shows that the NQC implementation should be revised for large spins, since

⁸ The same code is going to be released also via **LALSimulation**.

⁹ By contrast, let us remind that the standalone **TEOBResumS C** code can optionally output several dynamical quantities.

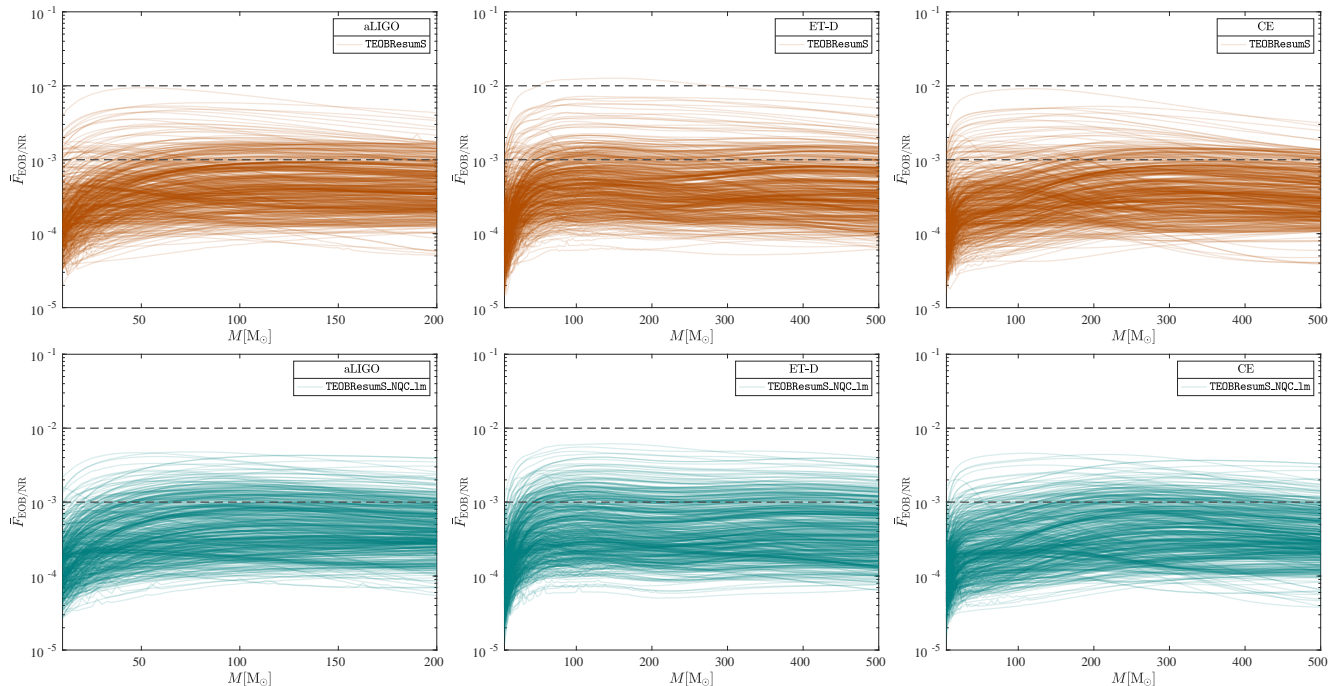


FIG. 12. EOB/NR unfaithfulness for `TEOBResumS` (top panels) and `TEOBResumS_NQC_1m` (bottom panels) evaluated over the sample of 534 nonprecessing quasicircular datasets of the SXS catalog already considered in Ref. [57], using: (i) the zero-detuned, high-power noise spectral density of Advanced LIGO (first column), (ii) the latest version of the expected noise for the Einstein Telescope (second column), (iii) the expected noise for Cosmic Explorer (third column). We observe here how the changes implemented in the new version of our model ensure a slight decrease in $\bar{F}_{\text{EOB/NR}}$, whose average is between 10^{-3} and 10^{-4} .

it introduces nonnegligible differences already during the inspiral¹⁰ (see also Appendix A).

The differences between the `SEOBNRv4HM` and NR fluxes remain large also in the other two cases (bottom row of Fig. 15). Given the many structural differences between the `SEOBNRv4HM` and `TEOBResumS` models, it is difficult to precisely track what are the elements within `SEOBNRv4HM` that are responsible of the flux behavior. The lack of the NQC factor in the `SEOBNRv4HM` flux is seemingly not enough to explain the differences that appear in the bottom panels of Fig. 15, since the `SEOBNRv4HM` curve differs even from the NQC-free flux of `TEOBResumS`. Let us mention at least two other differences that may be relevant in strong field. First of all, although the `SEOBNRv4HM` flux shares the same formal functional form of the `TEOBResumS` one, the definition of r_ω is different (see e.g. [11]). In addition, the PN truncation and the resummation of each waveform multipole, including the quadrupole one, differs between one model and the other.

B. Waveform amplitude and frequency

Let us now provide a direct comparison between `TEOBResumS`, `SEOBNRv4HM` and NR waveforms for the configurations considered above. We focus on the $\ell = m = 2$ waveform amplitude and frequency. Figure 15 contrasts the EOB/NR performance for `TEOBResumS` (left panels) and `SEOBNRv4HM` (right panels). The figure focuses around merger time and the waveforms are aligned in the late inspiral, just before merger. We recall that among the configurations presented in the figure, only the $(2, +0.85, +0.85)$ was used to inform c_3 for `TEOBResumS` and similarly only this was used to calibrate the spin sector of `SEOBNRv4HM` [47]. Both models deliver an excellent agreement with the NR waveform amplitude and frequency. However, there are relevant differences in the underlying dynamics, as suggested by the behavior of twice the orbital frequency, 2Ω , that is also displayed on the figure. In particular one sees that while for `TEOBResumS` $\omega_{22\text{EOB}} \simeq 2\Omega$ is always true up to the merger point, for `SEOBNRv4HM` this is approximately true only for the $(2, -0.6, +0.6)$ configuration. For the other cases, the dynamics seems to point to a delayed plunge, but the NR calibration of the `SEOBNRv4HM` model manages to have the analytical waveform on top of the NR one. Let us remember in fact that Ref. [47] also calibrates the time shift between the EOB orbital frequency and the peak

¹⁰ As already suggested in Ref. [16] it would be better to see the NQC corrections as an effective way of improving the EOB analytical waveform only very close to merger, and as such they should be progressively switched on only during the plunge.

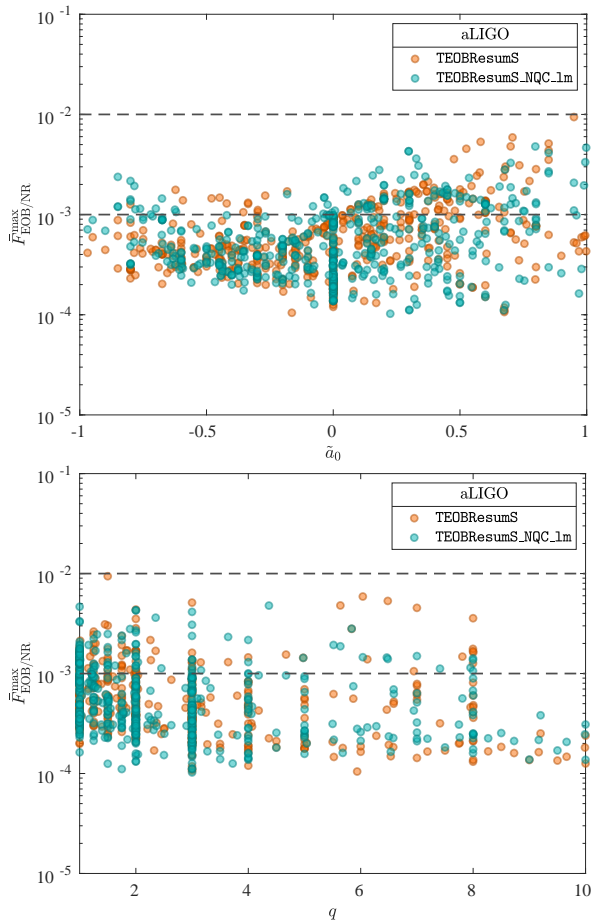


FIG. 13. Contrasting $\bar{F}_{\text{EOB/NR}}^{\text{max}}$ for TEOBResumS and TEOBResumS_NQC_1m versus \tilde{a}_0 and q , using the PSD of Advanced LIGO. This complements the top panels of Fig. 12.

of the EOB waveform where NQC corrections are determined and the ringdown attached. This feature is not needed in the TEOBResumS model, that uses as natural anchor point to determine NQC corrections the peak of the *pure* orbital frequency¹¹ Ω_{orb} (also shown in the figure), a quantity that is obtained subtracting the spin-orbit contribution from the total frequency. This structure is the effective generalization to the comparable-mass case of what is found in the test-mass limit [42], where the maximum of Ω_{orb} is always very close to the peak of the $\ell = m = 2$ waveform amplitude, as we also remind in Fig. 17 below.

¹¹ In fact, we use $t_{\text{NQC}} = t_{\Omega_{\text{orb}}}^{\text{peak}} - 1$, see in particular Eqs. (3.46)-(3.47) of Ref. [56] and Eqs. (102)-(105) and (108) of Ref. [42].

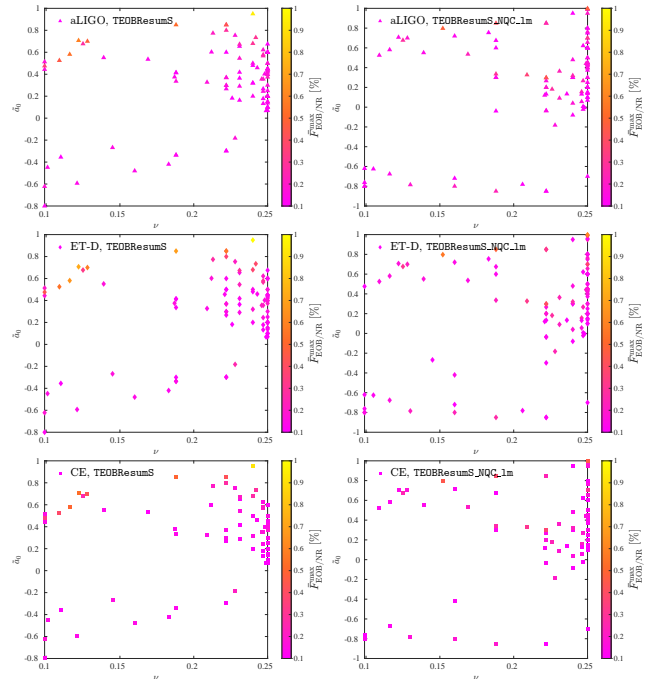


FIG. 14. Distribution over the parameter space (ν, \tilde{a}_0) of those configurations whose $\bar{F}_{\text{EOB/NR}}^{\text{max}}$ exceeds 10^{-3} , for aLIGO (first row), ET-D (second row), CE (third row), both for TEOBResumS (left column) and its updated version (right column). Notably, the changes implemented in TEOBResumS_NQC_1m lower the maximum unfaithfulness, although we see that higher values of the spin remain the most challenging ones to be modeled, along with the comparable-mass case.

1. The large-mass-ratio limit

Let us now consider the case of binary black hole coalescences in the large mass ratio limit and highlight the qualitative and quantitative features that are shared by TEOBResumS. Figure 17 shows amplitude and frequencies for a nonspinning test-particle (used to model the smaller black hole) inspiralling and plunging in the equatorial plane of a Kerr black hole. The analytical waveforms are generated using the test-mass limit version of TEOBResumS presented in Ref. [63], while the numerical waveforms are computed using the 2+1 time-domain code *Teukode* [64] that solves the Teukolsky equation (see also Ref. [65, 66] for an earlier EOB model in the test-particle limit). Note that, as usual, the dynamics generating the EOB and Teukolsky waveforms is the same. The analytical/numerical comparisons show that the condition $\omega_{22} \simeq 2\Omega$ is satisfied throughout the full evolution of the binary up to merger¹². Figure 17 collects

¹² For $\hat{a} < 0$ we have mode-mixing in the ringdown waveform but this is not relevant for the discussion of this paper.

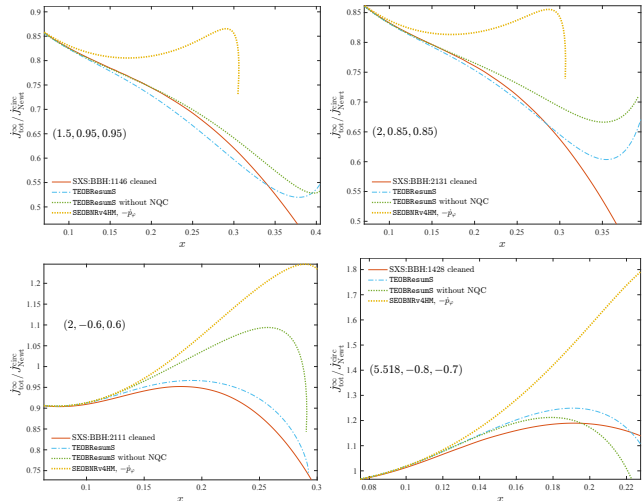


FIG. 15. For the configurations corresponding to simulations SXS:BBH:1146, SXS:BBH:2131, SXS:BBH:2111, SXS:BBH:1428 we show several angular momentum fluxes: (i) the NR one (orange), (ii) the TEOBResumS one (dash-dotted light blue), (iii) the TEOBResumS one without the NQC correction in the $\ell = m = 2$ mode (dash-dotted green), (iii) the corresponding flux from SEOBv4HM computed as $-\dot{p}_\varphi$ (dotted yellow).

a few, non extremal, values of the dimensionless Kerr parameter \hat{a} so to have a global view of the waveform phenomenology. It is useful to drive a qualitative and semi-quantitative comparison with Fig. 16. First, one notices the qualitative similarities between TEOBResumS and Teukolsky waveforms and dynamics, in particular the location of the peak of Ω_{orb} . This is a feature that was included within TEOBResumS by construction and seems to be one of the key points that allows one to have robust and consistent waveforms all over the parameter space. It is suggestive that the agreement is also semi quantitative for those cases that have $\hat{a} \simeq \hat{S}$. For example, the configuration with $\hat{S} = -0.2$ in Fig. 16 shows a behavior of Ω and Ω_{orb} that is qualitatively and quantitatively consistent with the $\hat{a} = -0.2$ case. Similarly, the $\hat{a} = 0.5$ configuration shows a behavior close to the ones with $\hat{S} = 0.47$ and $\hat{S} = 0.49$ (although the EOB frequency Ω does not deliver a local maximum), while the $\hat{a} = -0.6$ configuration is consistent with the $\hat{S} = -0.59$ one, with Ω becoming negative after merger. This similarity between test-mass and comparable-mass frequencies can be traced back to the quasi-universal behavior of ω_{22} at merger when plotted versus \hat{S} , already shown for NR data in Fig. 33 of Ref. [10]. Although at the moment this is nothing more than a suggestive semi-quantitative analogy, if taken seriously it could be helpful to further improve the dynamics of TEOBResumS and increase its consistency with the test-mass one, especially for high spins. The most obvious thing that needs to be improved is the frequency behavior for the shown high-spin configurations, (1.5, 0.95, 0.95) and (2, +0.85, +0.85), where Ω

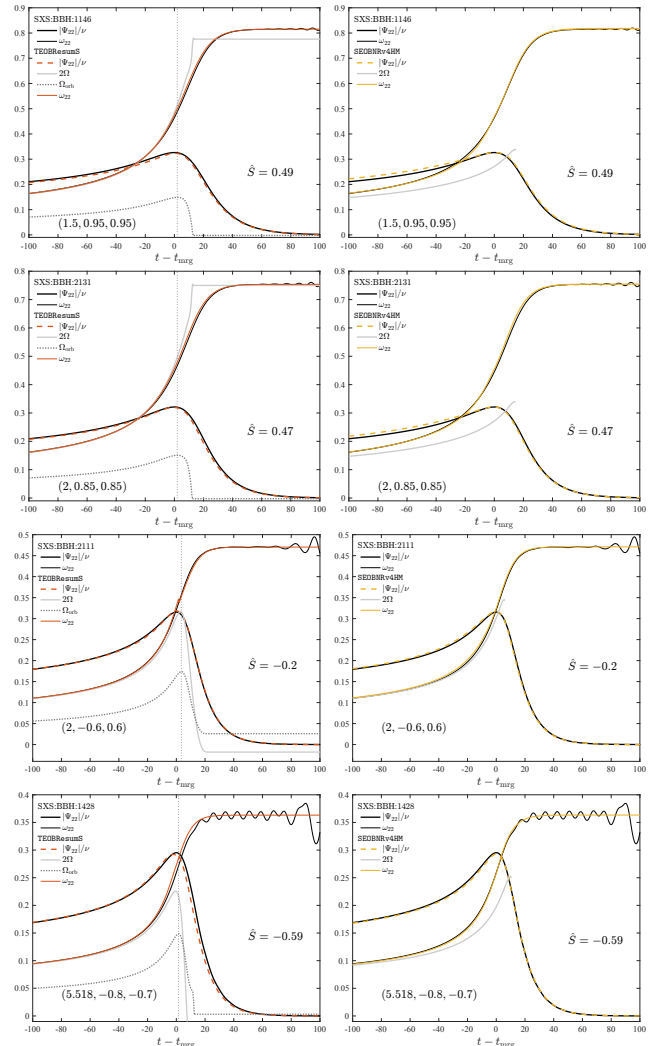


FIG. 16. Contrasting TEOBResumS (left) and SEOBv4HM (right). For each configuration we show: (i) the waveform amplitude, (ii) the instantaneous gravitational wave frequency, (iii) twice the orbital frequency Ω and (iv) the pure orbital frequency Ω_{orb} (i.e., without the spin-orbit contribution). Each binary is also labeled by its effective spin $\hat{S} \equiv (S_1 + S_2)/M^2$. For any configuration TEOBResumS maintains an excellent consistency between (twice) the orbital frequency and the gravitational wave frequency. This is especially true, as a priori expected, in the highly adiabatic cases with large positive spins where NQC corrections have a very limited effect. By contrast, for SEOBv4HM this holds only for the configuration (2, -0.6, 0.6). In the other cases, $\omega_{22} \neq 2\Omega$ and the correct behavior of the waveform frequency is guaranteed only by the action of NQC corrections.

keeps growing (until the evolution is stopped well after merger), which is in contrast with the local maximum present in the test-mass case for $\hat{a} = 0.5$ (and $\hat{a} = 0.7$ as well). This is related to the well known problem of the absence of a LSO in TEOBResumS for large, positive, spins and it might be solved using a different factorization and gauge for the spin-orbit sector [27]. Still, the

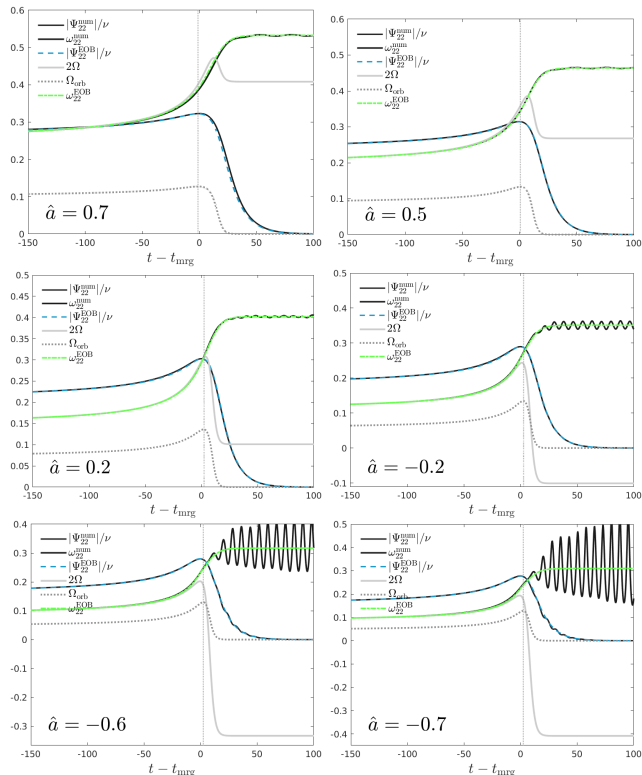


FIG. 17. Comparing EOB and numerical amplitude and frequencies in the large-mass-ratio limit ($\nu = 10^{-3}$) for different values of the Kerr dimensionless spin parameter \hat{a} . As can be seen, $\omega_{22} \simeq 2\Omega$ throughout the whole evolution up to merger. This behavior is also qualitatively shared by **TEOBResumS**, as shown in Fig. 16. We also show the reliability of the analytical prescription overlapping the EOB amplitudes and frequencies to numerical results.

current coherence between frequencies that is proper of **TEOBResumS** looks like an encouraging starting point for any future development.

C. Unfaithfulness

Let us finally move to the calculation of the EOB/NR unfaithfulness using the **SEOBNRv4HM** model. This calculation is not new, since it was done for the first time in Ref. [47] as test of the **SEOBNRv4** model. However, from Ref. [47] several *new* NR simulations offering a better covering of the parameter space became available and the original \bar{F} calculation was not updated since. In particular, updated comparisons don't seem to exist in Refs. [11, 14], nor in Ref. [67], that presents a faster version of the **SEOBNRv4HM** model based on the application of the post-adiabatic approximation developed in Ref. [9] (and notably already applied to the **SEOBNRv4HM** Hamiltonian in Ref. [27]). To our knowledge, it seems that $\bar{F}_{\text{EOB/NR}}$ has never been directly computed all over

the 534 spin-aligned datasets currently available¹³. It should be mentioned, though, that there exists a comparison between **SEOBNRv4HM** and the NR surrogate [22]. The purpose of this section is to complement the results of Ref. [22] via a direct comparison with the SXS datasets. To put this analysis into the right context, we present these results by contrasting them with the corresponding ones obtained using the *standard*, publicly available, *C* implementation of **TEOBResumS** already presented in Ref. [57]. Since this model relies on fits for the NQC corrections, as detailed in Ref. [57], its performance is slightly less good than the one we would obtain by using the (iterated) **MATLAB** implementation and similarly less good than what is theoretically achievable using **TEOBResumS_NQC_1m**. Figure 18 directly compares $\bar{F}_{\text{EOB/NR}}(M)$ from **TEOBResumS** (top panels) with the one from **SEOBNRv4HM** (bottom panels). The calculation is done for Advanced LIGO (first column), ET-D (second column) and CE (third column). The bottom-left panel of Fig. 18 is the analogous of Fig. 2 of Ref. [47], but with the additional SXS data that were not available at the time, and highlights the very different behavior of the two models for low masses, where **SEOBNRv4HM** grazes the 10^{-2} level for many configurations. This mirrors intrinsic structural differences, probably connected to the completely different way of deforming the Hamiltonian of a point-particle around a Kerr black hole implemented in the two models [27]. If this is acceptable for Advanced LIGO (although it evidences that the **SEOBNRv4HM** implementation is not accurate enough), it is not acceptable for ET-D or CE1, where **SEOBNRv4HM** grazes the 10^{-2} level for many configurations. Concerning the requirements for third generation detectors, Ref. [59] concluded that current EOB models are not yet sufficiently accurate. Our analysis shows that things look better by at least one order of magnitude for **TEOBResumS** or **TEOBResumS_NQC_1m**, that thus represent more encouraging starting points for developing highly faithful waveform models. Coming back to the Advanced LIGO design sensitivity curve, the results of the two left panels of Fig. 18 are further summarized in Fig. 19, that shows the corresponding $\bar{F}_{\text{EOB/NR}}^{\text{max}}$ either versus \tilde{a}_0 or versus q . Again, **TEOBResumS** is quite robust all over the parameter space, although its performance worsens when the effective spin is increased. This clearly indicates where the model needs to be improved further, coherently with the discussion made in the sections above. By contrast, this structure is absent for **SEOBNRv4HM** points, that look randomly distributed all over the parameter space.

¹³ The actual number of nonprecessing quasicircular datasets is larger but we do not consider some problematic simulations.

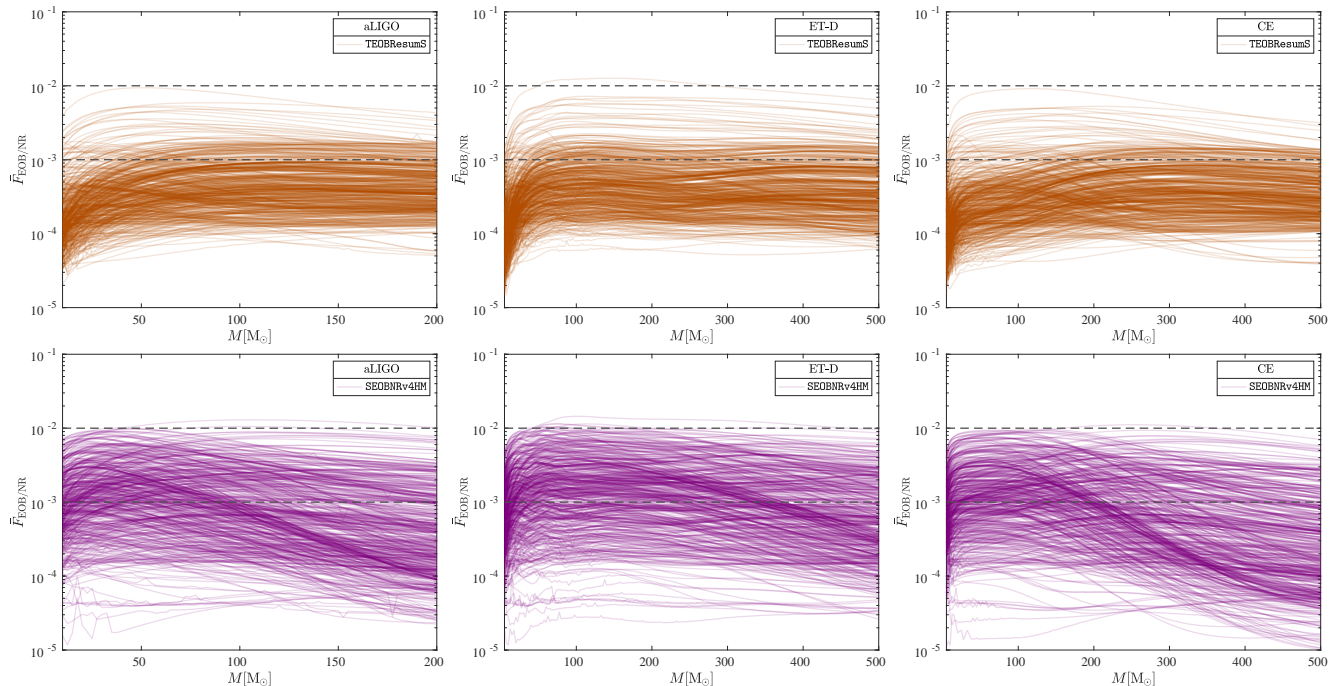


FIG. 18. Direct EOB/NR unfaithfulness comparison using the standard implementation of **TEOBResumS** (top panels) and **SEOBNRv4HM** (bottom panels). Again, the unfaithfulness is evaluated for the sample of 534 nonprecessing quasicircular NR simulations of the SXS catalog (likewise Fig. 12) using: (i) the zero-detuned, high-power noise spectral density of Advanced LIGO (first column), (ii) the expected PSD for Einstein Telescope (second column), (iii) the expected PSD for Cosmic Explorer (third column).

VI. CONCLUSIONS

We have presented an updated version of the spin-aligned waveform model **TEOBResumS** that differs from the previous ones for (i) a more careful procedure to inform the spin sector of the model, including new choices for NR simulations and a different functional form for the fit of the effective spin-orbit parameter c_3 , (ii) a specific effort to improve the behavior of the radiation reaction up to merger. In particular, our main achievement is to show that a careful inclusion of NQC corrections in the flux typically allows to achieve a EOB/NR flux consistency below 1% during the plunge. The consequent recalibration of the spin-orbit sector eventually grants a model that shows a higher NR-faithfulness all over the NR-covered parameter space. In addition we have provided the first ever detailed comparison between **TEOBResumS** and **SEOBNRv4HM**. Our results can be summarized as follows.

- (i) We have presented a novel computation of the angular momentum flux from a selected sample of 36 SXS datasets chosen so as to give a meaningful coverage of the full NR parameter space. Apparently, ours is the first computation of this kind from the early exploration of Ref. [34]. We have introduced an efficient procedure to remove low-frequency oscillations that are present in the raw fluxes obtained

directly from the data. Such oscillations, if kept, would prevent us to perform quantitatively accurate EOB/NR comparisons when the fluxes are represented as functions of the frequency.

- (ii) We have shown that the radiation reaction included in the standard implementation of **TEOBResumS** [13, 57] already exhibits an excellent consistency with the NR fluxes. However, this can be further improved by including NQC flux corrections in all $\ell = m$ modes up to $\ell = 5$.
- (iii) This modification to the radiation reaction effectively defined a *new* model, called **TEOBResumS_NQC_1m**, that also required us to update the determination of the NR-informed effective spin-orbit parameter c_3 . We did so by choosing a *new* sample of SXS NR datasets, many of which have improved accuracy with respect to the ones used in previous work. We evaluated the performance of this model all over the 534 spin-aligned SXS simulations available, using the Advanced LIGO PSD as well as the ones of ET and CE. To our knowledge, this is the first time an EOB model is being extensively tested for 3G detectors. We found that $\bar{F}_{\text{EOB/NR}}$ is within 10^{-4} and 10^{-3} for more than 80% of the considered binaries. The outliers always occur

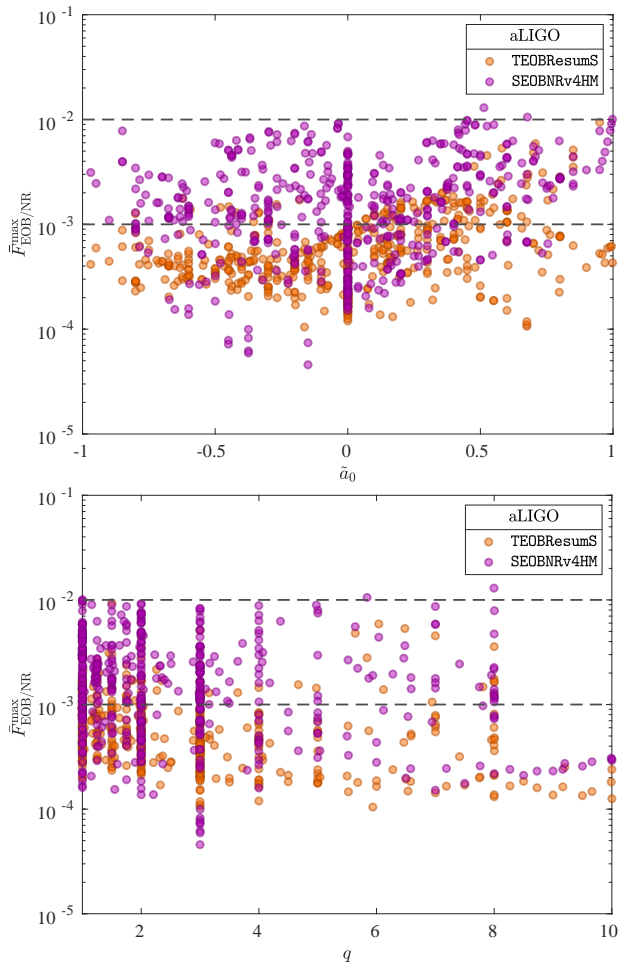


FIG. 19. Contrasting $\bar{F}_{\text{EOB/NR}}^{\text{max}}$ for TEOBResumS and SEOBNRv4HM versus \tilde{a}_0 and ν . The values for TEOBResumS are smaller than those of SEOBNRv4HM, and also show a clear dependence on the effective spin, indicating where the model may need further improvements.

for configurations with large, positive, spins, that are the most difficult to simulate numerically and to model analytically. Although we are still far from the expected 3G detector calibration error, between $\sim 10^{-4}$ and $\sim 10^{-5}$, our analysis shows that (any version of) TEOBResumS can already be used for 3G-related studies provided the spin parameters are not too extreme. In our opinion, it might be possible that the increase in accuracy needed for 3G detectors advocated in Ref. [59] will be less dramatic than suggested.

- (iv) By contrast, when the same analyses are performed on the SEOBNRv4HM EOB waveform model, we find large differences between the analytical and numerical fluxes for a restricted sample of dataset for which, however, TEOBResumS is NR-consistent already in its native form. For the same configurations we also considered waveform and frequen-

cies comparisons, underlining how the dynamics of TEOBResumS is qualitatively consistent with the expectations coming from test-particle limit calculations. Similarly, we show that for the same configurations the dynamics of SEOBNRv4HM, differently from the one of TEOBResumS, is qualitatively inconsistent with the expectations coming from test-particle limit calculations. We finally fill the apparent gap in the literature of the calculation of the EOB/NR unfaithfulness for the $\ell = m = 2$ mode over all the 534 spin-aligned SXS NR simulations available, for Advanced LIGO, ET-D and CE detectors. The outcome of this calculation is directly contrasted with the corresponding one from the standard version of TEOBResumS, highlighting the different performance of the two models, especially during the inspiral. This is worth noticing because TEOBResumS and SEOBNRv4HM were built using similar strategies and the same original PN information¹⁴.

The most important take-away message of our work is that TEOBResumS can be improved (especially in the large-spin sector) only by means of minimal modifications to its structure and a more careful choice of the NR simulations used to inform the model. In this respect, it is worth mentioning that the available NR simulations could be better exploited to inform both a_6^c and c_3 . To maintain continuity with previous work, we did not change the function describing a_6^c and we anchored the fit of c_3 to the equal-mass case, using 16 equal-mass SXS dataset, while only additional 20 are used to determine the function up to $q = 8$. This was motivated by the fact that in the past the SXS collaboration mainly focused on producing equal-mass binaries. Nowadays things have changed, and in particular there are many dataset available with $q = 4$, since they were needed to construct a NR waveform surrogate NRSur7dq4 [71]. Since we are using only 2 dataset with $q \simeq 4$, an improved model would be obtained by just anchoring the c_3 fit to more $q = 4$ simulations, possibly with also an improved choice of a_6^c more carefully exploiting the nonspinning datasets. We expect that this will additionally improve the EOB/NR agreement, possibly pushing it below the 10^{-4} level for all binaries. This seems to be at reach given the simplicity and minimality of our procedures and will be tackled in future work.

¹⁴ Actually, SEOBNRv4HM includes the exact spin-orbit sector of a spinning test-body [68–70], while it is only approximated within TEOBResumS. It is however straightforward to build a TEOBResumS-like Hamiltonian with the exact spinning test-body limit included [27].

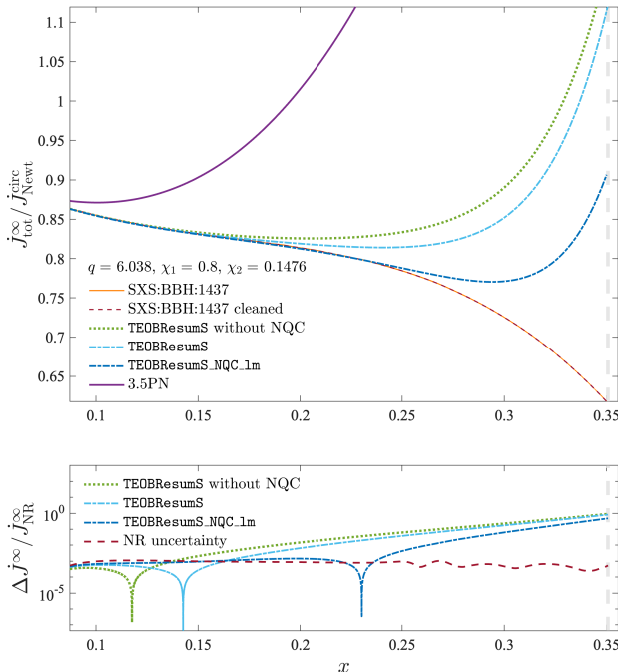


FIG. 20. Contrasting EOB/NR total fluxes summed up to $\ell = 8$ using either `TEOBResumS` or `TEOBResumS_NQC_1m` for the dataset SXS:BBH:1437, with $(q, \chi_1, \chi_2) = (6.038, 0.8, 0.1476)$. The addition of NQC corrections increases the EOB/NR agreement, though it is not sufficient to completely remove the growing behavior at the end of the evolution. As seen in Fig. 8, for `TEOBResumS_NQC_1m` the multipoles up to $\ell = m = 5$ are consistent with the numerical flux, meaning that the improvement is only needed for modes with $\ell \geq 6$.

ACKNOWLEDGMENTS

A.A. has been supported by the fellowship Luminaria Quaeruntur No. LQ100032102 of the Czech Academy of Sciences. We are grateful to M. Breschi for a careful reading of the manuscript, and to S. Bernuzzi for daily discussions and for the music. The `TEOBResumS` code is publicly available at https://bitbucket.org/eob_ihes/teobresums/. The v2 version of the code, that implements the PA approximation and higher modes, is fully documented in Refs. [9, 12, 13, 57, 72]. We recommend the above references to be cited by `TEOBResumS` users.

Appendix A: Issues in the NQC-corrected fluxes

In this section we focus on some problematic EOB fluxes. Let us start by considering the dataset SXS:BBH:1437. As seen in Fig. 20, for this configuration the additions of NQC corrections increases the agreement with NR but does not avoid the growing behavior at the end of the evolution. As pointed out in Fig. 8, for `TEOBResumS_NQC_1m` the EOB flux is consistent with the numerical one up to $\ell = m = 5$, so this behavior this is

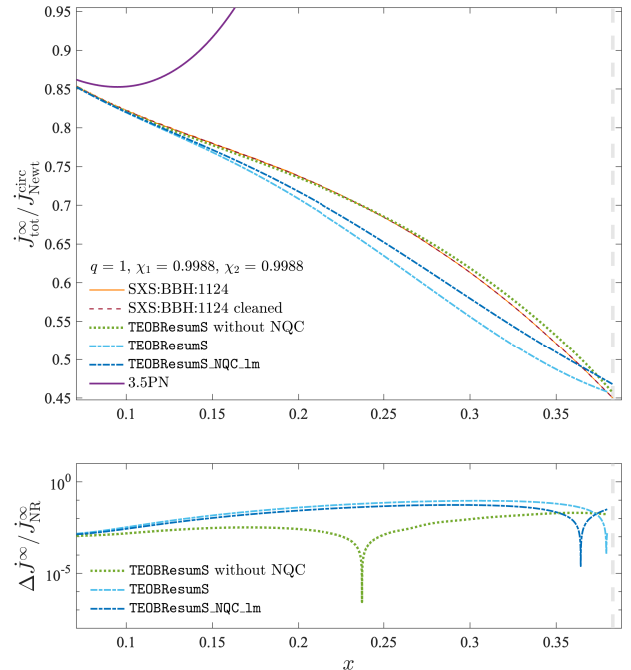


FIG. 21. Contrasting EOB/NR fluxes for the configuration $(q, \chi_1, \chi_2) = (1, 0.9988, 0.9988)$, corresponding to dataset SXS:BBH:1124. The flux without NQC corrections is more consistent with the numerical one with respect to the NQC-corrected ones, both from `TEOBResumS` and from `TEOBResumS_NQC_1m`.

due to modes with $6 \leq \ell \leq 8$, that only rely on analytical information and do not incorporate NQC corrections. Nevertheless, we underline that the EOB/NR relative difference for `TEOBResumS_NQC_1m` is of order 10^{-3} until $x \sim 0.24$, corresponding to ~ 1.5 orbits before merger.

Let us now consider dataset SXS:BBH:1124, corresponding to the extremely spinning configuration $(q, \chi_1, \chi_2) = (1, 0.9988, 0.9988)$. In this case the purely analytical flux is in excellent agreement with the NR one, keeping the fractional difference below 10^{-2} until merger, but surprisingly NQC corrections worsen the flux behavior all over the evolution. This may be attributed to two different facts: (i) the motion for a comparable mass binary with such high spins is highly adiabatic, so that there is a reduced need of non-circular correction factors; (ii) NQC corrections in the current model are added from the beginning of the evolution, considering they are functions of the radial momentum which is small but non-negligible during the inspiral, and its effect is progressively amplified. To avoid this issue it seems better to include the NQC factor only as a correction that is progressively switched on towards merger, similarly to what is currently implemented in the version of `TEOBResumS` valid for noncircular configurations [17, 18].

Finally, we consider the two datasets excluded from the bottom panel of Fig. 9, namely SXS:BBH:1419 and SXS:BBH:1375, respectively corresponding to $(q, \chi_1, \chi_2) = (8, -0.80, -0.80)$ and $(q, \chi_1, \chi_2) =$

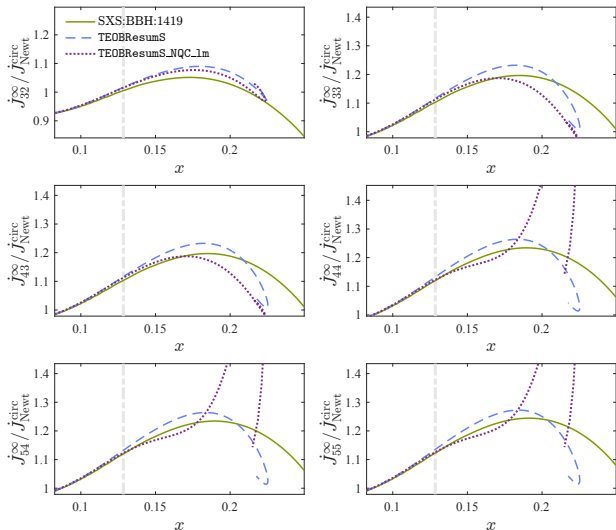


FIG. 22. Comparison between EOB/NR fluxes for one of the configurations excluded from Fig. 9, SXS:BBH:1419, with $(q, \chi_1, \chi_2) = (8, -0.8, -0.8)$. In this case the NQC correction factor in the $\ell = m = 4$ mode becomes pathological and eventually TEOBResumS yields a more NR-consistent flux.

$(8, -0.90, 0)$. The multipolar fluxes for the first configuration are shown in Fig. 22, from which we infer that the NQC correction factor is not correctly determined for the $\ell = m = 4$ and $\ell = m = 5$ modes, with the former multipole yielding the largest deviations. One notices, however, that up to the $\ell = m = 4$ mode excluded, NQC corrections yield an agreement between the fluxes up to the LSO that is closer than the standard case. The same happens for the dataset SXS:BBH:1375. We also found that for $(8, -0.80, -0.80)$ it is possible to fix the behavior of the $\ell = m = 4$ mode by adjusting the c_3 value from the value predicted by the fit, $c_3^{\text{fit}} = 65.16$, to $c_3 = 77$. On the contrary, this is not possible for $(8, -0.90, 0)$, indicating that a more detailed understanding of the determination of the NQC corrections is needed in this case.

Appendix B: Improving the consistency between waveform and flux changing Newtonian prefactors

Let us finally present an EOB/NR flux comparison using a model that has $\ell = m$ NQC corrections in the flux up to $\ell = 5$ and uses *consistent* Newtonian prefactors in the flux and in the waveform. In practice, this amounts at replacing $v_\Omega = \Omega^{1/3}$ with the standard v_φ in Eqs. (3.22)-(3.30) in Sec. IIIC of Ref. [12]. As can be seen in Fig. 23, this actually yields a more consistent flux for the con-

figuration corresponding to dataset SXS:BBH:1436 we analyzed previously. But, not surprisingly, this does not hold for the problematic corner of the parameter space that motivated the different choice for the Newtonian prefactors in the waveform, as evident when looking at the values in Table IV. Moreover, we noticed there are

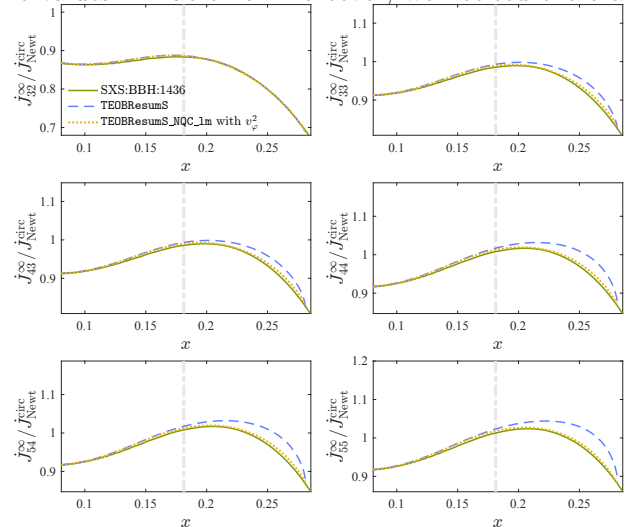


FIG. 23. Comparing EOB/NR multipolar fluxes for the dataset SXS:BBH:1436, using TEOBResumS_NQC_1m with the standard Newtonian prefactors in the waveform written as powers of v_φ (see text). For this configuration, this choice yields an excellent EOB/NR agreement up to merger.

some configurations, e.g. $(8, -0.8, -0.8)$, in which even the $\ell = m = 2$ multipole is spoiled by the unsuccessful determination of NQC corrections.

For future developments, the EOB/NR flux agreement in Fig. 23 encourages us to look for different solutions to ensure the NQC determination works out for high mass ratios and negative spins.

Appendix C: Unfaithfulness with the ET-C noise

We display in this section results for the EOB/NR unfaithfulness computation by using the less recent PSD of Einstein Telescope, ET-C [44]. As one can see in Fig. 11, ET-D has a larger sensitivity with respect to ET-C for higher frequencies, where we expect both EOB and NR waveforms to be less accurate¹⁵. Correspondently, the results shown in Fig. 24 and in Table V are slightly better than the ones we reported above for the latest PSD, probably also owing to the fact that viceversa the ET-C version has a larger sensitivity at lower frequencies.

¹⁵ This is related as well to the choice of the extrapolation order and the ringdown modeling, as discussed above.

TABLE IV. EOB/NR fractional flux differences at $x = 0.2$, both for `TEOBResumS_NQC_lm` and for its waveform/flux consistent version.

| ID | (q, χ_1, χ_2) | $\Delta j_{\text{EOBNR}}^{\text{NQC_lm}}$ | $\Delta j_{\text{EOBNR}}^{v_\varphi^2}$ |
|----------|------------------------|--|---|
| BBH:1155 | (1, 0, 0) | 0.001957 | 0.0022517 |
| BBH:1222 | (2, 0, 0) | -0.0001001 | 0.002563 |
| BBH:1179 | (3, 0, 0) | -0.00071698 | 0.0040221 |
| BBH:0190 | (4.499, 0, 0) | -0.0084789 | -0.0021009 |
| BBH:0192 | (6.58, 0, 0) | -0.0098679 | -0.0030977 |
| BBH:1107 | (10, 0, 0) | -0.011246 | -0.0096363 |
| BBH:1137 | (1, -0.97, -0.97) | 0.099337 | - |
| BBH:2084 | (1, -0.90, 0) | 0.072879 | 0.038549 |
| BBH:2097 | (1, +0.30, 0) | -0.0032907 | -0.0029234 |
| BBH:2105 | (1, +0.90, 0) | -0.01013 | -0.011484 |
| BBH:1124 | (1, +0.99, +0.99) | -0.0272 | -0.027025 |
| BBH:1146 | (1.5, +0.95, +0.95) | -0.035553 | -0.035553 |
| BBH:2111 | (2, -0.60, +0.60) | 0.015314 | 0.017929 |
| BBH:2124 | (2, +0.30, 0) | -0.0061851 | -0.0044956 |
| BBH:2131 | (2, +0.85, +0.85) | -0.01893 | -0.018629 |
| BBH:2132 | (2, +0.87, 0) | -0.011947 | -0.010621 |
| BBH:2133 | (3, -0.73, +0.85) | 0.031988 | 0.03876 |
| BBH:2153 | (3, +0.30, 0) | -0.0042875 | -0.0012004 |
| BBH:2162 | (3, +0.60, +0.40) | -0.011459 | -0.0097236 |
| BBH:1446 | (3.154, -0.80, +0.78) | 0.04242 | 0.049673 |
| BBH:1936 | (4, -0.80, -0.80) | 0.051971 | - |
| BBH:2040 | (4, -0.80, -0.40) | 0.048942 | 0.063711 |
| BBH:1911 | (4, 0, -0.80) | 0.0019117 | 0.0083588 |
| BBH:2014 | (4, +0.80, +0.40) | -0.0089473 | -0.0078338 |
| BBH:1434 | (4.368, +0.80, +0.80) | -0.012975 | -0.01188 |
| BBH:1463 | (4.978, +0.61, +0.24) | -0.0083662 | -0.0064106 |
| BBH:0208 | (5, -0.90, 0) | 0.037164 | 0.0016289 |
| BBH:1428 | (5.518, -0.80, -0.70) | 0.030081 | - |
| BBH:1437 | (6.038, +0.80, +0.15) | -0.001383 | -0.00033034 |
| BBH:1436 | (6.281, +0.009, -0.80) | -0.002271 | 0.0041482 |
| BBH:1435 | (6.588, -0.79, +0.7) | 0.0054703 | - |
| BBH:1448 | (6.944, -0.48, +0.52) | 0.0091571 | 0.42486 |
| BBH:1375 | (8, -0.90, 0) | 1.3589 | - |
| BBH:1419 | (8, -0.80, -0.80) | 0.19952 | - |
| BBH:1420 | (8, -0.80, +0.80) | -0.022786 | - |
| BBH:1455 | (8, -0.40, 0) | 0.0070483 | 0.27028 |

[1] F. Acernese et al. (VIRGO), *Class. Quant. Grav.* **32**, 024001 (2015), arXiv:1408.3978 [gr-qc].
[2] J. Aasi et al. (LIGO Scientific), *Class. Quant. Grav.* **32**, 074001 (2015), arXiv:1411.4547 [gr-qc].
[3] R. Abbott et al. (LIGO Scientific, Virgo), *Phys. Rev. X* **11**, 021053 (2021), arXiv:2010.14527 [gr-qc].

[4] A. Buonanno and T. Damour, *Phys. Rev.* **D59**, 084006 (1999), arXiv:gr-qc/9811091.
[5] A. Buonanno and T. Damour, *Phys. Rev.* **D62**, 064015 (2000), arXiv:gr-qc/0001013.
[6] T. Damour, P. Jaranowski, and G. Schaefel, *Phys. Rev.* **D62**, 084011 (2000), arXiv:gr-qc/0005034 [gr-qc].

TABLE V. Analogous of Table III, using the ET-C power spectral density. The central columns of the table display the fraction of datasets whose maximum unfaithfulness $\bar{F}_{\text{EOB/NR}}^{\text{max}}$ is within the indicated limits for **TEOBResumS**, **TEOBResumS_NQC_1m** or **SEOBNRv4HM**. Again, as in Table III, the last two columns display percentage numbers out of *all* the mismatch values.

| | $\bar{F}^{\text{max}} < 10^{-3}$ | $10^{-3} < \bar{F}^{\text{max}} < 10^{-2}$ | $\bar{F}^{\text{max}} > 3 \times 10^{-3}$ | $10^{-4} < \bar{F} < 10^{-3}$ | $\bar{F} < 10^{-4}$ |
|--------------------------|----------------------------------|--|---|-------------------------------|---------------------|
| TEOBResumS | 85.0% | 14.4% | 2.6% | 84.5% | 5.3% |
| TEOBResumS_NQC_1m | 82.4% | 18.0% | 1.7% | 81.1% | 6.9% |
| SEOBNRv4HM | 36.3% | 38.0% | 27.7% | 48.1% | 3.2% |

- [7] T. Damour, Phys. Rev. **D64**, 124013 (2001), arXiv:gr-qc/0103018.
- [8] T. Damour, P. Jaranowski, and G. Schäfer, Phys. Rev. **D91**, 084024 (2015), arXiv:1502.07245 [gr-qc].
- [9] A. Nagar and P. Retegno, Phys. Rev. **D99**, 021501 (2019), arXiv:1805.03891 [gr-qc].
- [10] A. Nagar et al., Phys. Rev. **D98**, 104052 (2018), arXiv:1806.01772 [gr-qc].
- [11] R. Cotesta, A. Buonanno, A. Bohé, A. Taracchini, I. Hinder, and S. Ossokine, Phys. Rev. **D98**, 084028 (2018), arXiv:1803.10701 [gr-qc].
- [12] A. Nagar, G. Pratten, G. Riemenschneider, and R. Gamba, (2019), arXiv:1904.09550 [gr-qc].
- [13] A. Nagar, G. Riemenschneider, G. Pratten, P. Retegno, and F. Messina, Phys. Rev. D **102**, 024077 (2020), arXiv:2001.09082 [gr-qc].
- [14] S. Ossokine et al., Phys. Rev. D **102**, 044055 (2020), arXiv:2004.09442 [gr-qc].
- [15] S. Schmidt, M. Breschi, R. Gamba, G. Pagano, P. Retegno, G. Riemenschneider, S. Bernuzzi, A. Nagar, and W. Del Pozzo, Phys. Rev. D **103**, 043020 (2021), arXiv:2011.01958 [gr-qc].
- [16] D. Chiaramello and A. Nagar, Phys. Rev. D **101**, 101501 (2020), arXiv:2001.11736 [gr-qc].
- [17] A. Nagar, A. Bonino, and P. Retegno, Phys. Rev. D **103**, 104021 (2021), arXiv:2101.08624 [gr-qc].
- [18] A. Nagar and P. Retegno, (2021), arXiv:2108.02043 [gr-qc].
- [19] T. Damour, F. Guercilena, I. Hinder, S. Hopper, A. Nagar, et al., (2014), arXiv:1402.7307 [gr-qc].
- [20] A. Nagar, P. Retegno, R. Gamba, and S. Bernuzzi, Phys. Rev. D **103**, 064013 (2021), arXiv:2009.12857 [gr-qc].
- [21] R. Gamba, M. Breschi, G. Carullo, P. Retegno, S. Albanesi, S. Bernuzzi, and A. Nagar, Submitted to Nature Astronomy (2021), arXiv:2106.05575 [gr-qc].
- [22] G. Pratten, S. Husa, C. Garcia-Quiros, M. Colleoni, A. Ramos-Buades, H. Estelles, and R. Jaume, Phys. Rev. D **102**, 064001 (2020), arXiv:2001.11412 [gr-qc].
- [23] C. García-Quirós, M. Colleoni, S. Husa, H. Estellés, G. Pratten, A. Ramos-Buades, M. Mateu-Lucena, and R. Jaume, Phys. Rev. D **102**, 064002 (2020), arXiv:2001.10914 [gr-qc].
- [24] G. Pratten et al., Phys. Rev. D **103**, 104056 (2021), arXiv:2004.06503 [gr-qc].
- [25] S. Akçay, R. Gamba, and S. Bernuzzi, Phys. Rev. D **103**, 024014 (2021), arXiv:2005.05338 [gr-qc].
- [26] R. Gamba, S. Akçay, S. Bernuzzi, and J. Williams, (2021), arXiv:2111.03675 [gr-qc].
- [27] P. Retegno, F. Martinetti, A. Nagar, D. Bini, G. Riemenschneider, and T. Damour, (2019), arXiv:1911.10818 [gr-qc].
- [28] T. Damour, A. Nagar, D. Pollney, and C. Reisswig, Phys. Rev. Lett. **108**, 131101 (2012), arXiv:1110.2938 [gr-qc].
- [29] A. Nagar, T. Damour, C. Reisswig, and D. Pollney, Phys. Rev. **D93**, 044046 (2016), arXiv:1506.08457 [gr-qc].
- [30] S. Ossokine, T. Dietrich, E. Foley, R. Katebi, and G. Lovelace, Phys. Rev. **D98**, 104057 (2018), arXiv:1712.06533 [gr-qc].
- [31] A. Le Tiec, A. H. Mroue, L. Barack, A. Buonanno, H. P. Pfeiffer, N. Sago, and A. Taracchini, Phys. Rev. Lett. **107**, 141101 (2011), arXiv:1106.3278 [gr-qc].
- [32] A. Le Tiec et al., Phys. Rev. D **88**, 124027 (2013), arXiv:1309.0541 [gr-qc].
- [33] T. Hinderer et al., Phys. Rev. **D88**, 084005 (2013), arXiv:1309.0544 [gr-qc].
- [34] M. Boyle, A. Buonanno, L. E. Kidder, A. H. Mroue, Y. Pan, et al., Phys. Rev. **D78**, 104020 (2008), arXiv:0804.4184 [gr-qc].
- [35] M. Boyle et al., Class. Quant. Grav. **36**, 195006 (2019), arXiv:1904.04831 [gr-qc].
- [36] D. Reitze et al., (2021), arXiv:2111.06986 [gr-qc].
- [37] P. Couvares et al., (2021), arXiv:2111.06987 [gr-qc].
- [38] M. Punturo et al., (2021), arXiv:2111.06988 [gr-qc].
- [39] S. Katsanevas et al., (2021), arXiv:2111.06989 [gr-qc].
- [40] V. Kalogera et al., (2021), arXiv:2111.06990 [gr-qc].
- [41] D. McClelland et al., (2021), arXiv:2111.06991 [gr-qc].
- [42] T. Damour and A. Nagar, Phys. Rev. **D90**, 044018 (2014), arXiv:1406.6913 [gr-qc].
- [43] “Updated Advanced LIGO sensitivity design curve,” <https://dcc.ligo.org/LIGO-T1800044/public>.
- [44] S. Hild, S. Chelkowski, A. Freise, J. Franc, N. Morgado, R. Flaminio, and R. DeSalvo, Class. Quant. Grav. **27**, 015003 (2010), arXiv:0906.2655 [gr-qc].
- [45] S. Hild et al., Class. Quant. Grav. **28**, 094013 (2011), arXiv:1012.0908 [gr-qc].
- [46] M. Evans et al., (2021), arXiv:2109.09882 [astro-ph.IM].
- [47] A. Bohé et al., Phys. Rev. **D95**, 044028 (2017), arXiv:1611.03703 [gr-qc].
- [48] R. Cotesta, S. Marsat, and M. Pürrer, Phys. Rev. D **101**, 124040 (2020), arXiv:2003.12079 [gr-qc].
- [49] K. Mitman et al., Phys. Rev. D **104**, 024051 (2021), arXiv:2105.02300 [gr-qc].
- [50] M. Campanelli, C. Lousto, and Y. Zlochower, Phys. Rev. **D74**, 041501 (2006), arXiv:gr-qc/0604012 [gr-qc].
- [51] D. Bini and T. Damour, Phys. Rev. **D86**, 124012 (2012), arXiv:1210.2834 [gr-qc].

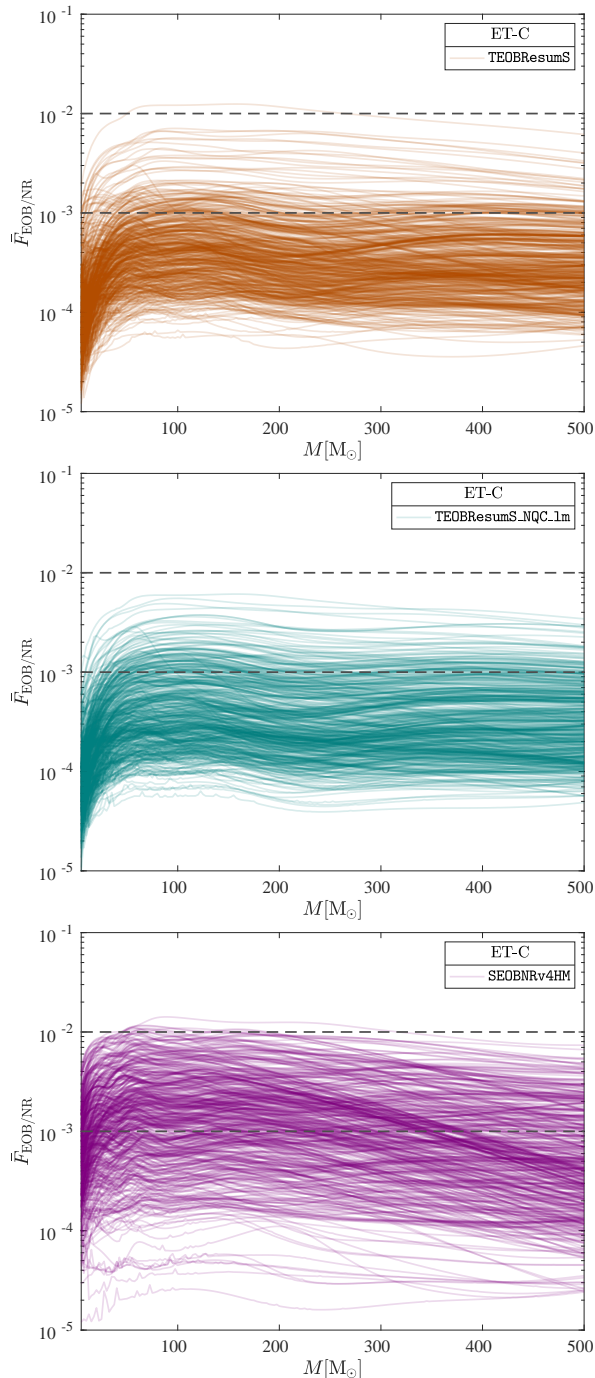


FIG. 24. EOB/NR unfaithfulness for TEOBResumS (top), TEOBResumS_NQC_1m (middle) and SEOBNRv4HM (bottom), evaluated using the ET-C version of the expected noise for Einstein Telescope [44].

- [52] T. Damour and A. Gopakumar, Phys. Rev. **D73**, 124006 (2006), arXiv:gr-qc/0602117.
- [53] T. Damour and A. Nagar, Phys. Rev. **D76**, 064028 (2007), arXiv:0705.2519 [gr-qc].
- [54] T. Damour, A. Nagar, and S. Bernuzzi, Phys. Rev. **D87**, 084035 (2013), arXiv:1212.4357 [gr-qc].
- [55] T. Damour, B. R. Iyer, and A. Nagar, Phys. Rev. **D79**, 064004 (2009), arXiv:0811.2069 [gr-qc].
- [56] A. Nagar, G. Riemenschneider, and G. Pratten, Phys. Rev. **D96**, 084045 (2017), arXiv:1703.06814 [gr-qc].
- [57] G. Riemenschneider, P. Retegno, M. Breschi, A. Albertini, R. Gamba, S. Bernuzzi, and A. Nagar, Phys. Rev. **D104**, 104045 (2021), arXiv:2104.07533 [gr-qc].
- [58] T. Damour and A. Nagar, Phys. Rev. **D79**, 081503 (2009), arXiv:0902.0136 [gr-qc].
- [59] M. Pürrer and C.-J. Haster, Phys. Rev. Res. **2**, 023151 (2020), arXiv:1912.10055 [gr-qc].
- [60] J. Moxon, M. A. Scheel, S. A. Teukolsky, N. Deppe, N. Fischer, F. Hébert, L. E. Kidder, and W. Throwe, (2021), arXiv:2110.08635 [gr-qc].
- [61] N. L. Fischer et al., (2021), arXiv:2111.06767 [gr-qc].
- [62] L. M. n. Zertuche et al., (2021), arXiv:2110.15922 [gr-qc].
- [63] S. Albanesi, A. Nagar, and S. Bernuzzi, Phys. Rev. **D104**, 024067 (2021), arXiv:2104.10559 [gr-qc].
- [64] E. Harms, S. Bernuzzi, A. Nagar, and A. Zenginoglu, Class. Quant. Grav. **31**, 245004 (2014), arXiv:1406.5983 [gr-qc].
- [65] E. Barausse, A. Buonanno, S. A. Hughes, G. Khanna, S. O'Sullivan, et al., Phys. Rev. **D85**, 024046 (2012), arXiv:1110.3081 [gr-qc].
- [66] A. Taracchini, A. Buonanno, S. A. Hughes, and G. Khanna, Phys. Rev. **D88**, 044001 (2013), arXiv:1305.2184 [gr-qc].
- [67] D. P. Mihaylov, S. Ossokine, A. Buonanno, and A. Ghosh, (2021), arXiv:2105.06983 [gr-qc].
- [68] E. Barausse, E. Racine, and A. Buonanno, Phys. Rev. **D80**, 104025 (2009), arXiv:0907.4745 [gr-qc].
- [69] E. Barausse and A. Buonanno, Phys. Rev. **D81**, 084024 (2010), arXiv:0912.3517 [gr-qc].
- [70] E. Barausse and A. Buonanno, Phys. Rev. **D84**, 104027 (2011), arXiv:1107.2904 [gr-qc].
- [71] V. Varma, S. E. Field, M. A. Scheel, J. Blackman, D. Gerosa, L. C. Stein, L. E. Kidder, and H. P. Pfeiffer, Phys. Rev. Research. **1**, 033015 (2019), arXiv:1905.09300 [gr-qc].
- [72] A. Nagar, F. Messina, P. Retegno, D. Bini, T. Damour, A. Gericco, S. Akcay, and S. Bernuzzi, Phys. Rev. **D99**, 044007 (2019), arXiv:1812.07923 [gr-qc].